THE GLOBAL ICOSAHEDRAL-HEXAGONAL GRID POINT MODEL GME - OPERATIONAL VERSION AND HIGH RESOLUTION TESTS -

Detlev Majewski, Dörte Liermann, Peter Prohl and Bodo Ritter
Michael Buchhold, Thomas Hanisch, Gerhard Paul und Werner Wergen
Deutscher Wetterdienst, Research and Development Division, Offenbach, Germany

John Baumgardner
Los Alamos National Laboratory, Los Alamos, New Mexico, USA

1. INTRODUCTION

Motivated by trends in numerical methods and high performance computing architectures the Deutscher Wetterdienst (DWD) has developed a new operational global numerical weather prediction (NWP) model that employs a grid point approach with an almost uniform icosahedral-hexagonal grid. On 1st December 1999, this new model has replaced the operational global model GM, derived from the spectral model of the European Centre for Medium Range Weather Forecasts (ECMWF), and the regional model EM for central Europe. It has been named GME.

The grid point approach offers several important advantages relative to spectral methods. One is elimination of "spectral ringing" in the vicinity of steep gradients. Another is the ability to insure positivity in quantities such as cloud liquid water and turbulent kinetic energy. The grid point approach also avoids the large amount of global communication required by spectral transform techniques as well as the large number of arithmetic operations normally associated with Legendre transforms at high spatial resolution.

A major advantage of the icosahedral-hexagonal grid is the avoidance of the so-called 'pole problem' that exists in conventional latitude-longitude grids. The singularities at the poles lead to a variety of numerical difficulties including a severe limitation on the time step size unless special measures are undertaken. These difficulties simply vanish for grids not having such singularities.

Icosahedral-hexagonal grids were investigated more than thirty years ago for their suitability to meteorological application. Williamson (1968) and Sadourny et al. (1968) solved the nondivergent barotropic vorticity equation with finite difference methods on such grids. Later, Cullen (1974) applied a finite element approach and a similar grid to solve the shallow water equations. The conclusions from these initial investigations, however, was that the discretization error arising from the slight grid non-uniformities was sufficiently large to render this grid point approach inferior to the then emerging spectral transform method. In the early 1980's Baumgardner (1983) and Baumgardner and Frederickson (1985) devised recursively defined spherical barycentric coordinates that provided spherical basis

functions from which a fully second-order accurate finite element formulation could be obtained. Second order convergence was demonstrated in both the two and infinity norms. Since that time his finite element approach has been successfully applied to modelling planetary mantle convection in spherical shell geometry (Baumgardner, 1985)

In the early 1990's Baumgardner, in collaboration with a colleague John Dukowicz at Los Alamos National Laboratory, developed a second-order accurate semi-Lagrangian formulation for the shallow water equations on the icosahedral-hexagonal grid (Baumgardner, 1995). This formulation utilised basis functions obtained by constructing a local spherical coordinate system at each grid point with the grid point located at the coordinate frame equator. Since these coordinate systems are utilised only in the local neighbourhood of a grid point, the far removed polar singularities introduce no difficulties. GME employs this same set of basis functions that correspond simply to the longitude and latitude in the local grid point coordinate frame.

Other investigators who have applied an icosahedral-hexagonal grid in an atmospheric modelling context include Masuda and Ohnishi (1986), Heikes and Randall (1995a,b), and Stuhne and Peltier (1996, 1999). Masuda and Ohnishi applied a finite difference approach to solve the shallow water equations in stream function/velocity potential form with the finite difference operators derived from a line integral method. Heikes and Randall used an almost identical approach except that they introduce a 'twist' in the grid to make it symmetrical across the equatorial plane and they employ a multigrid strategy for solving elliptic equations for the streamfunction and velocity potential. They also introduced a scheme for moving the grid points slightly to reduce the errors in their finite difference operators. Stuhne and Peltier, on the other hand, applied a method very close to that of Baumgardner and Frederickson (1985) for solving the elliptic equations via a finite element/multigrid strategy with recursively defined barycentric basis functions but chose a finite difference strategy similar to Baumgardner (1995) for discretizing first derivative operators. The main difference in the latter strategy from Baumgardner is their use of Cartesian coordinates and local basis functions that lie in a plane tangent to the sphere at each grid point instead of local spherical coordinates and spherical basis functions.

None of the more recent formulations that achieve second-order accuracy (e.g., Baumgardner and Frederickson, 1985; Heikes and Randall, 1995a, b; Baumgardner, 1995; Stuhne and Peltier, 1996, 1999) displays the significant wave number five error that plagued the early formulations using the icosahedral-hexagonal grid. We are convinced that the explanation for the large error in the earlier formulations was simply the low order of their spatial discretization.

A first description of the design and implementation of the GME, including shallow water tests and an evaluation of the dynamical core of the model, is given in Majewski (1998); here we concentrate on the operational version of the model and tests at high resolutions.

The outline of the paper is as follows: Section 2 describes the basic numerical methods including the grid generation, formulation of the discrete operators, and an evaluation of their accuracy. In section 3 the three-dimensional version of GME, including the physical parameterization package, is described. Section 4 provides an overview of the data assimilation scheme, section 5 describes the operational implementation at the DWD, and section 6 presents some results of diagnostics and verification of the model. Finally, section 7 summarises the first results of 24-h forecasts of the GME at mesh sizes between 160 and 15 km.

2. NUMERICAL METHODS

2.1 Grid Generation

The icosahedral-hexagonal grid, first introduced in meteorological modelling by Sadourny et al. (1968) and Williamson (1968), has been gaining increasing interest in recent years, e.g. Masuda and Ohnishi (1987), Heikes and Randall (1995 a, b), Giraldo (1997) and Thuburn (1997). The approach described here closely follows the work of Baumgardner (1983) who has applied this grid to the problem of planetary mantle convection.

To generate the grid, a regular icosahedron (Fig. 1) is constructed inside the sphere such that two of its twelve vertices coincide with the north and south poles. Five of the other ten vertices are spaced at equal longitudinal intervals of 72° (= 360°/5) along a latitude circle at 26.565°N, the other five along a latitude circle at 26.565°S.

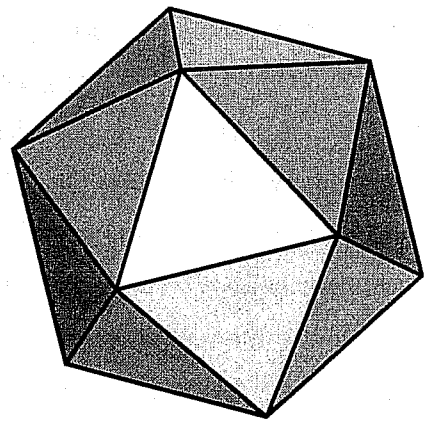

Figure 1 Regular icosahedron which consists of 20 equilateral triangles.

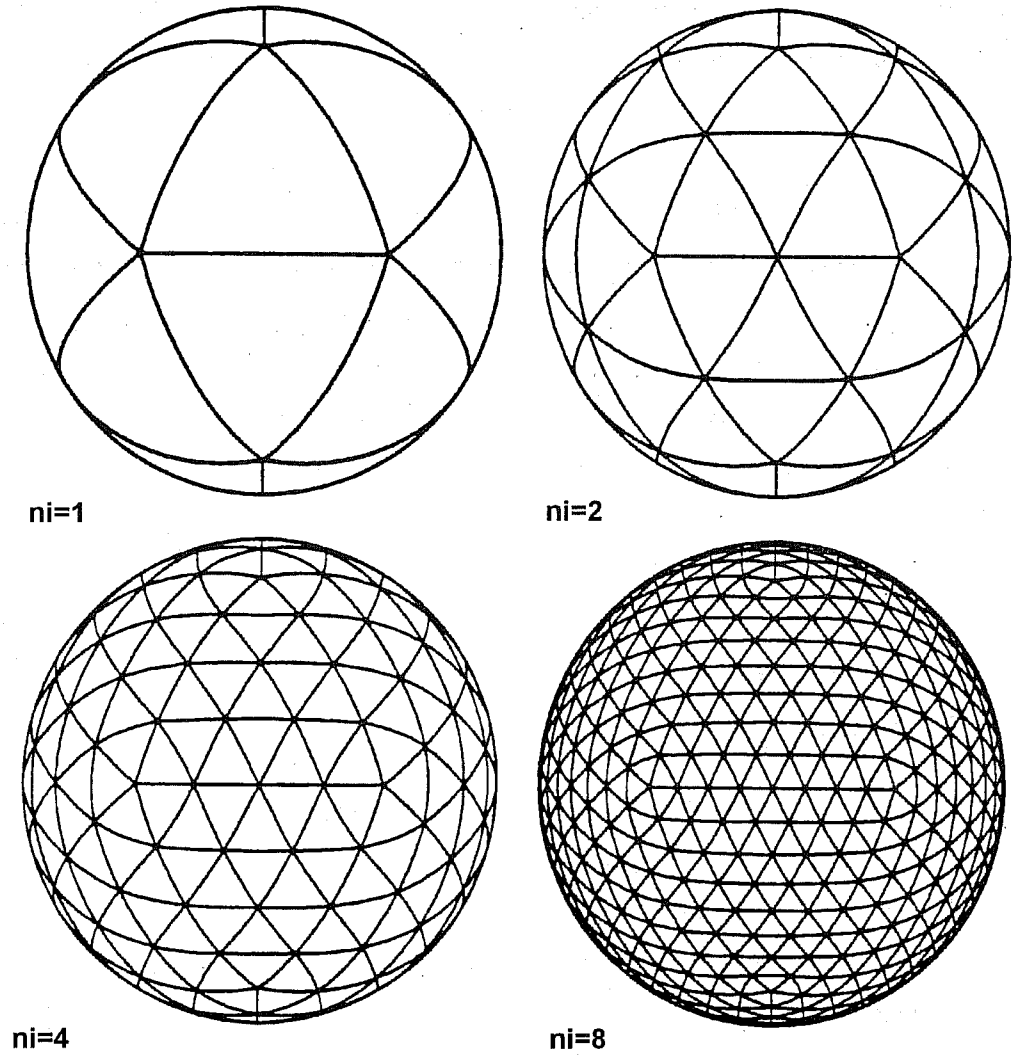

Figure 2 Grid generation by successively halving the triangle edges to form new triangles. Parameter *ni* is the number of intervals on a major triangle edge (length ~ 7054 km).

Connecting nearest neighbours among these twelve points with great circle arcs divides the spherical surface into 20 equal spherical triangles (Fig. 2, top left). Beginning from this grid of icosahedral triangles, a new finer grid of triangles is generated by connecting midpoints of the spherical triangle sides by an additional set of great circle arcs (Fig. 2, top right). This process may be repeated until a grid of the desired resolution is obtained. This construction procedure yields a grid consisting of $10\ n_i^2 + 2$ grid points (nodes) and $20\ n_i^2$ elementary spherical triangles, where n_i is the number of equal intervals into which each side of the original icosahedral triangles is divided. Each of these $10\ n_i^2 + 2$ grid points is surrounded by six nearest neighbours except for the original twelve icosahedral vertices which are surrounded by only five. We therefore refer to these twelve special points as *pentagonal* points. The dual mesh to the triangular one we have just described consists exclusively of hexagons except for the twelve pentagons at the pentagonal points (Fig. 3).

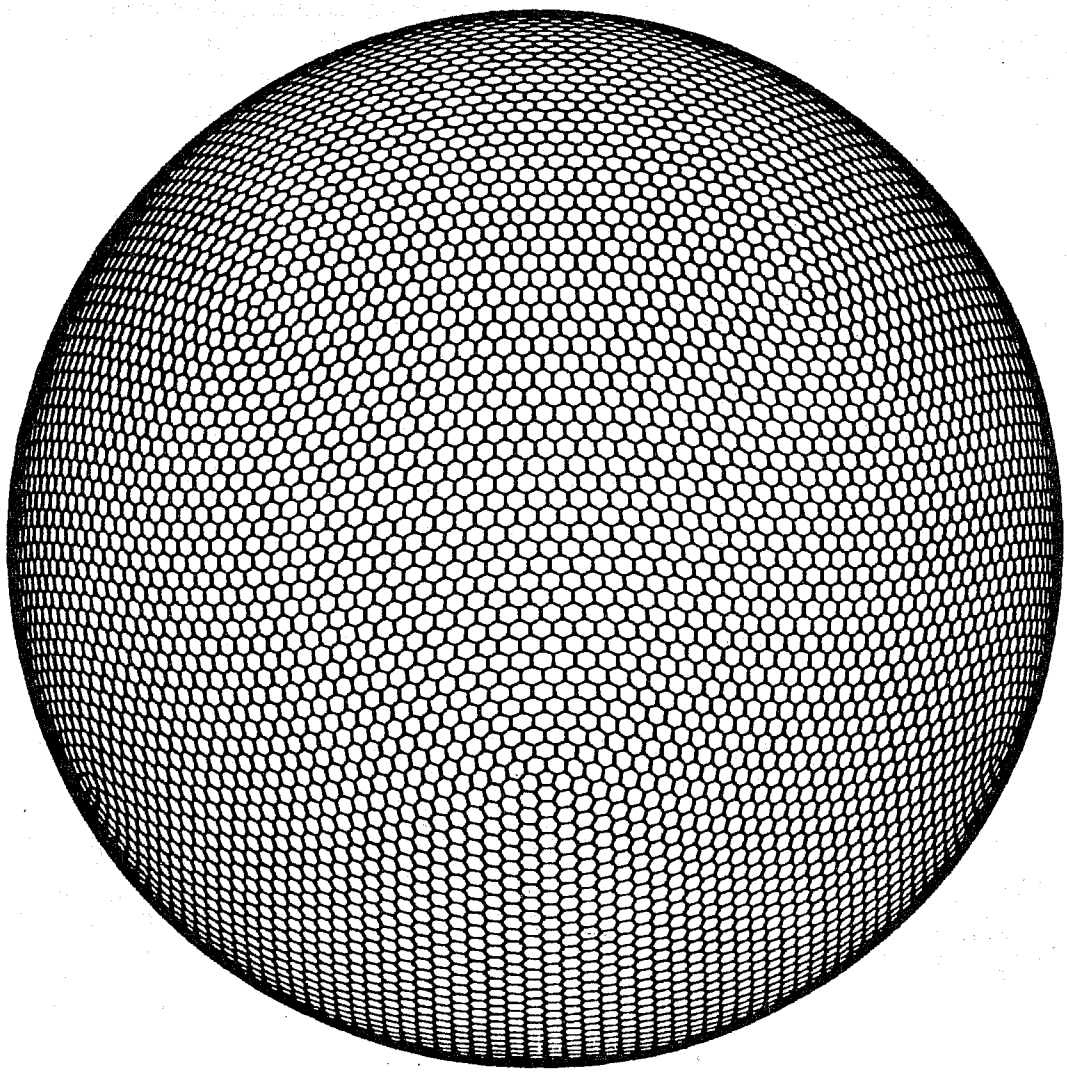

Figure 3 The grid points of GME represent nearly uniform hexagons (pentagons at the twelve special points); in this figure, there are three pentagons visible.

The number n_i is a natural parameter for specifying the resolution of the grid. It can be shown that there is a close numerical equivalence between n_i and the maximum harmonic degree in a spherical harmonic representation. The (minimum) spacing between grid points is then the length of a side of the original icosahedral triangles (about 7054 km for the earth) divided by n_i. For example, with n_i = 128 we obtain a spacing between grid points of about 55 km.

The icosahedral-hexagonal grid provides a nearly uniform coverage of the sphere even though the hexagonal cells vary somewhat in their exact shape and size (Table 1a), especially those close to the pentagons. The pentagons, however, are perfectly regular. To increase the available choice of grid resolution, an initial trisection of the main triangles edges followed by bisections may be performed. Specifications for these grids are summarised in Table 1b.

Table 1 Some characteristic quantities of the icosahedral-hexagonal grid at different resolutions specified by n_i, the number of intervals on a major triangle edge. Here, $N = 10\,n_i^2 + 2$ is the number of grid points, A_{min} is the minimum area of the hexagons, A_{max} is the maximum area of the hexagons; Δ_{av} is the average distance between grid points; Δ_{min} is the minimum distance between grid points; and Δ_{max} is the maximum distance between grid points.

Table 1a Sides of icosahedral triangles are each bisected q times, i.e. $n_i = 2^q$, where q is a positive integer.

q	n_i	N	A_{min} (km^2)	A_{max} (km^2)	Δ_{av} (km)	Δ_{min} (km)	Δ_{max} (km)
4	16	2562	154109	238061	477.6	440.5	526.0
5	32	10242	38515	59955	239.3	220.3	263.2
6	64	40962	9628	15017	119.8	110.1	131.6
7	128	163842	2407	3756	59.9	55.1	65.8
8	256	655362	602	939	30.0	27.6	32.9
9	512	2621442	150	235	15.0	13.8	16.5

Table 1b Sides of icosahedral triangles are initially trisected, and then bisected l times, i.e., $n_i = 3 * 2^l = 2^q$, where $q = 1.585 + l$.

q	n_i	N	A_{min} (km^2)	A_{max} (km^2)	Δ_{av} (km)	Δ_{min} (km)	Δ_{max} (km)
4.6	24	5762	68477	97683	319.0	293.7	346.9
5.6	48	23042	17117	24494	159.7	146.8	173.5
6.6	96	92162	4279	6128	79.9	73.4	86.8
7.6	192	368642	1070	1532	40.0	36.7	43.4
8.6	384	1474562	267	383	20.0	18.4	21.7
9.6	768	5898242	67	96	10.0	9.2	10.9

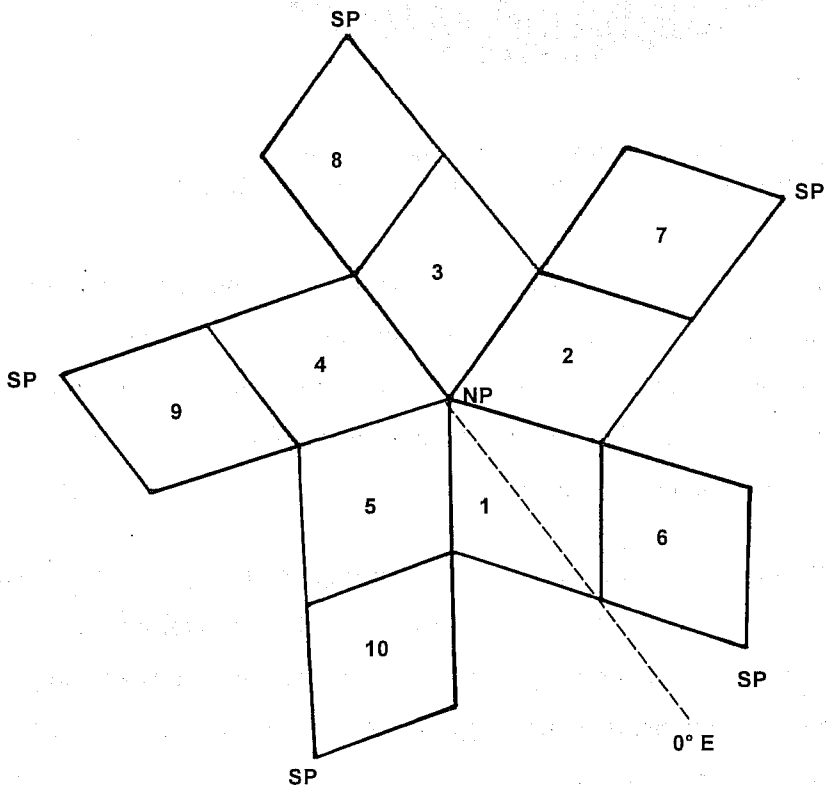

Figure 4 Logical data layout of the icosahedral-hexagonal grid of GME consisting of ten rhombi (diamonds), five containing the north pole and five the south pole.

By combining the areas of pairs of the original adjacent icosahedral triangles, the global grid can logically also be viewed as comprised of ten rhombi or diamonds, each of which has n_i x n_i unique grid points. The diamonds are indexed as shown in Fig. 4. Five diamonds share the north pole and five the south pole. The indexing on a diamond is based on the convention that those n_i x n_i grid points which are unique to each diamond are numbered from *1* to n_i in the rows and columns of the data arrays as shown in Fig. 5. The grid points on the diamonds edges, *(0,1)* to *(0, n_i+1)* and *(0, n_i+1)* to *(n_i, n_i+1)*, are shared between adjacent diamonds and their data values must be exchanged at each time step. The polar points *(0,1)* are each shared by five diamonds. Diamonds 1 to 5 share the north pole and diamonds 6 to 10 share the south pole.

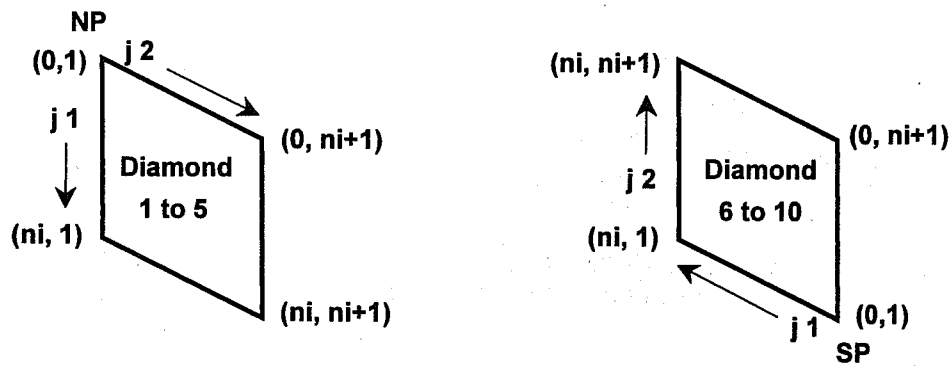

Figure 5 Indexing the grid points within one diamond; on the left for diamonds 1 to 5 which originate at the north pole, on the right for diamonds 6 to 10 which originate at the south pole.

From the computational point of view the icosahedral-hexagonal grid offers the major advantage that no indirect addressing is required. The data structure is regular and has the dimensions (0: n_i, n_i+1,10), i.e., consists of ten logically square arrays of points. Discrete differential operators have the form of seven point stencils, involving the home point and the six nearest neighbour points. The indices of the neighbour points are given by fixed offsets from the index of the home point. These operations can be coded to obtain high efficiencies on both vector and cache-based computer architectures. Furthermore, the square arrays of points are readily partitioned in a domain decomposition strategy for distributed memory parallel architectures.

2.2 Horizontal Finite Difference Operators

The derivation of finite-difference operators is not based on Gauss´ theorem as in Masuda and Ohnishi (1987) or Heikes and Randall (1995) but follows a strategy similar to that of Stuhne and Peltier (1996, 1999). Our approach utilises local basis functions that are orthogonal and conform perfectly to the spherical surface. These basis functions are the longitude and latitude of a locally defined spherical coordinate system whose equator and zero meridian intersect at the grid point. We generate such a local spherical coordinate system at each grid point with coordinates (η , χ) and align the local east direction to coincide with the global east direction and the local north with the global north direction.

The local spherical coordinate system is specified by three orthogonal unit vectors $[\mathbf{x}_0, (\mathbf{e}_\lambda)_0, (\mathbf{e}_\varphi)_0]$, where $\mathbf{x}_0$ is the grid point location on the unit sphere, $(\mathbf{e}_\lambda)_0$ is orthogonal to $\mathbf{x}_0$ and aligned with the global east and $(\mathbf{e}_\varphi)_0$ is orthogonal to $\mathbf{x}_0$ and aligned with the global north direction (Fig. 6).

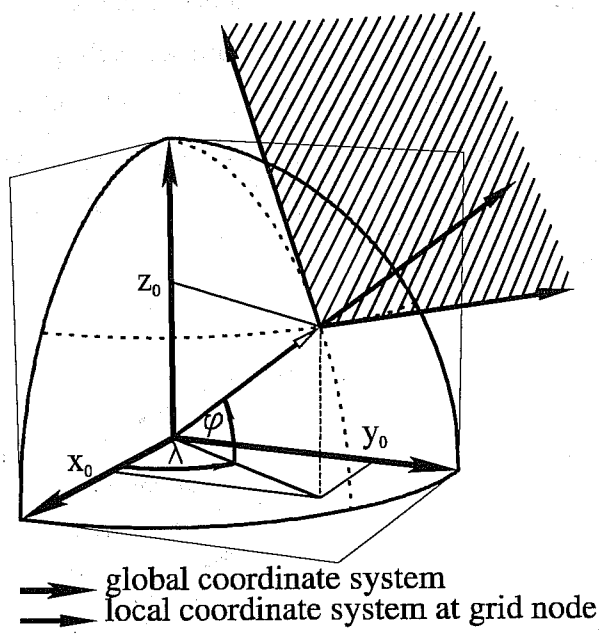

Figure 6 Global coordinate system (x, y, z) and local system (η, χ) at a grid point.

The advantages of this local coordinate system are

- Within the local neighbourhood of the grid point the coordinate system is nearly Cartesian, i.e., the coordinate singularities are far removed from this grid point neighbourhood; and
- only two (tangential) velocity components are needed to describe the horizontal velocities.

However, there is one disadvantage, namely, transformations are required between the local coordinate systems of neighbouring grid points when operators are applied to vector fields.

The meteorological equations are formulated and solved in the local spherical system (η, χ), where the horizontal distances (*dx, dy*) on the earth of radius *a* are given by $dx = a\cos\chi\, d\eta$ and $dy = a d\chi$.

Discrete horizontal operators must be derived for this system. The analytical form of the operators is the usual form as given for example by *Dutton* (1976) taking into account that $\eta = \chi = 0$ at the centre node.

2.2.1 Derivation of the Discrete Gradient and Laplace Operators

To obtain a second-order accurate representation of the partial differential equations we desire to solve, we approximate an arbitrary global function ψ^* in the neighbourhood of each grid point by a quadratic polynomial ψ in the local coordinates (η, χ) as

$$\psi(\eta,\chi)=\psi_0+\alpha_1\eta+\alpha_2\chi+\alpha_3\eta^2+\alpha_4\eta\chi+\alpha_5\chi^2 \tag{2.1}$$

Eq. (2.1) may be interpreted as a Taylor series of the form

$$\psi(\eta,\chi)=\psi_0+\left(\frac{\partial\psi}{\partial\eta}\right)\eta+\left(\frac{\partial\psi}{\partial\chi}\right)\chi+\frac{1}{2}\left(\frac{\partial^2\psi}{\partial\eta^2}\right)\eta^2+\left(\frac{\partial^2\psi}{\partial\eta\,\partial\chi}\right)\eta\chi+\frac{1}{2}\left(\frac{\partial^2\psi}{\partial\chi^2}\right)\chi^2 \tag{2.2}$$

The finite-difference form of the gradient and Laplace operators for a scalar field ψ may be written in terms of a stencil operation involving the values of ψ at the center node and the nearest five or six neighbours. (For simplicity in what follows, we shall let the neighbour index m range from 1 to 6 also in case of pentagonal nodes where it will be understood that the stencil coefficients for the non-existent node are identically zero.)

The gradient operator at each grid point may be expressed

$$\frac{\partial\psi}{\partial\eta}=\sum_{m=1}^{6}G_{\eta,m}(\psi_m-\psi_0) \tag{2.3}$$

$$\frac{\partial\psi}{\partial\chi}=\sum_{m=1}^{6}G_{\chi,m}(\psi_m-\psi_0) \tag{2.4}$$

The coefficients $G_{\eta,m}$, $G_{\chi,m}$ (m = 1,...,6) are associated with the neighbouring nodes and depend only on the geometric locations of the nodes expressed in terms of the local coordinates (η, χ). The numbering of the grid points is counterclockwise as shown in Fig. 7.

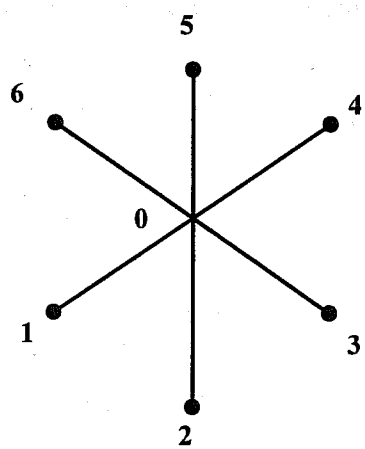

Figure 7 The central node (*0*) and the 6 surrounding neighbours (*1 to 6*) of a hexagon used by the elementary stencil of the icosahedral-hexagonal grid.

Similar to the approach for the gradient operator, the Laplace operator is expressed in terms of the neighbouring nodes as

$$\left(\frac{\partial^2}{\partial\eta^2}+\frac{\partial^2}{\partial\chi^2}\right)\psi=\sum_{m=1}^{6}L_m(\psi_m-\psi_0) \tag{2.5}$$

To obtain the stencil coefficients $G_{\eta,m}$, $G_{\chi,m}$, and L_m we apply the quadratic polynomial approximation (2.1). For the case of six nearest neighbours, we have six constraints for the five coefficients α_1, α_2, ..., α_5 that specify the function ψ in the local neighbourhood, namely,

$$\psi_m(\eta_m,\chi_m)=\psi_0+\alpha_1\eta_m+\alpha_2\chi_m+\alpha_3\eta_m^2+\alpha_4\eta_m\chi_m+\alpha_5\chi_m^2 \tag{2.6}$$

for m = 1,...,6. A least squares procedure is used to solve for the five unknown coefficients from a system of the form

$$\alpha_j=\beta_{j,m}(\psi_m-\psi_0) \tag{2.7}$$

where j = 1,...,5, and the summation is over m = 1,...,6.

Using Eqs. (2.1) through (2.6) the coefficients $G_{\eta,m}$, $G_{\chi,m}$ are then given by

$$G_{\eta,m}=\beta_{1,m} \qquad \text{and} \qquad G_{\chi,m}=\beta_{2,m} \tag{2.8}$$

and the coefficients L_m by

$$L_m=2(\beta_{3,m}+\beta_{5,m}) \tag{2.9}$$

where m = 1,...,6.

Due to the symmetry of the icosahedral-hexagonal grid, the coefficients $G_{\eta,m}$, $G_{\chi,m}$, and L_m may be precomputed and stored only for diamond 1. Since the divergence operator is simply the negative transpose of the gradient operator, we can use the same gradient coefficients to compute the velocity divergence. Care has to be taken, however, to rotate the wind components (u_m, v_m) of the surrounding nodes into the local spherical coordinate system of the central node before the divergence operator is applied.

2.3 Interpolation in the Icosahedral-Hexagonal Grid

GME uses semi-Lagrangian advection for water vapour and cloud water. Semi-Lagrangian methods require the interpolation of fields from neighbouring grid points to the departure and midpoints of the parcel trajectory. Our approach involves two types of interpolation, namely *bilinear* and *biquadratic*. *Bilinear* interpolation is used in the calculation of the trajectory itself to derive the wind components

(u, v) at the trajectory midpoint. *Biquadratic* interpolation is then applied to find the prognostic fields at the departure point of the trajectory. Both methods are performed on grid triangles.

2.3.1 Bilinear Interpolation

Bilinear interpolation of an arbitrary function $\psi(\eta,\chi)$ at a point $P(\eta,\chi)$ uses the values (ψ_0, ψ_1, ψ_2) at the three grid points (P_0, P_1, P_2) having position vectors (p_0, p_1, p_2) that are the vertices of the spherical triangle containing the point as indicated in Fig. 8.

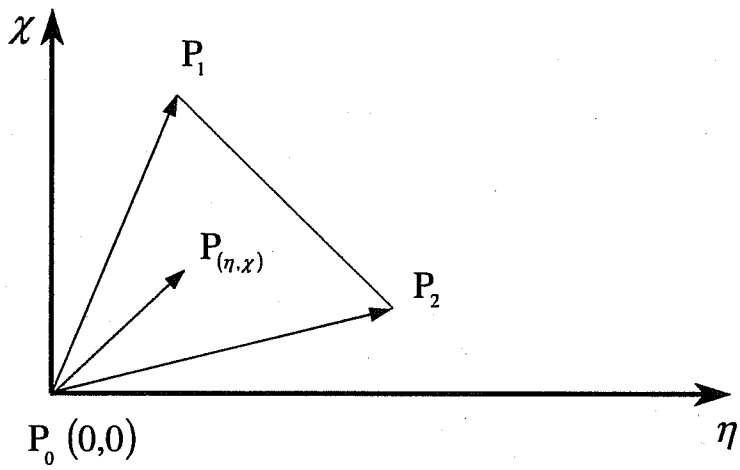

Figure 8 A triangle P_0, P_1, P_2 in the local spherical (η,χ) coordinate system.

To derive the value $\psi(\eta,\chi)$ at $P(\eta,\chi)$ we introduce barycentric coordinates. Each point within the triangle is uniquely defined by the vector

$$p = \gamma_0 p_0 + \gamma_1 p_1 + \gamma_2 p_2 \qquad \text{where} \qquad \gamma_0 + \gamma_1 + \gamma_2 = 1 \tag{2.10}$$

where (γ_0, γ_1, γ_2) are called the barycentric coordinates of the point P. To calculate these coordinates the following linear system has to be solved (note that at the central node P_0, $\eta = \chi = 0$):

$$\eta = \gamma_1\eta_1 + \gamma_2\eta_2 \qquad \text{and} \qquad \chi = \gamma_1\chi_1 + \gamma_2\chi_2 \qquad \text{and} \qquad \gamma_0 = 1 - \gamma_1 - \gamma_2 \tag{2.11}$$

The bilinear interpolation of $\psi(\eta,\chi)$ within the triangle is then obtained by weighting the values of ψ at the triangle vertices by the corresponding barycentric coordinates:

$$\psi(\eta,\chi) = \gamma_0\psi(\eta_0,\chi_0) + \gamma_1\psi(\eta_1,\chi_1) + \gamma_2\psi(\eta_2,\chi_2) \tag{2.12}$$

2.3.2 Biquadratic Interpolation

The standard biquadratic interpolation formula for a triangle in terms of values at the triangle vertices and midpoints of the edges (Fig.9) is applied to obtain the value of ψ at an arbitrary point $P(\eta,\chi)$ in the triangle:

$$\psi(\gamma_0,\gamma_1,\gamma_2)=\gamma_0(2\gamma_0-1)\psi_0+\gamma_1(2\gamma_1-1)\psi_1+\gamma_2(2\gamma_2-1)\psi_2+4(\gamma_0\gamma_1\psi_4+\gamma_1\gamma_2\psi_5+\gamma_2\gamma_0\psi_6) \quad (2.13)$$

where $(\gamma_0, \gamma_1, \gamma_2)$ are again the barycentric coordinates of the point P.

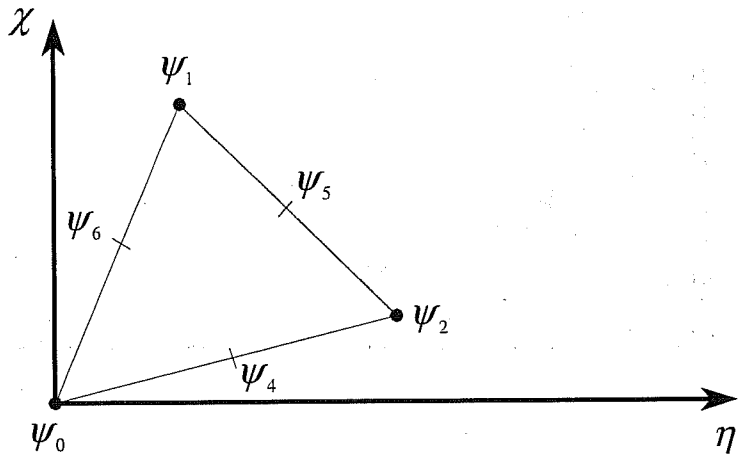

Figure 9 The six values used for the biquadratic interpolation of a function $\psi(\eta,\chi)$ in a triangle.

The values of the function ψ at the midpoints of the triangle edges, ψ_4, ψ_5, ψ_6, are obtained by approximating ψ along these edges with a cubic Hermite polynomial using the gradients at the end points, that is, at the triangle vertices (P_0, P_1, P_2). When the stencil of the gradient operator is taken into account, the biquadratic interpolation is based on a stencil that involves twelve grid points (Fig. 10).

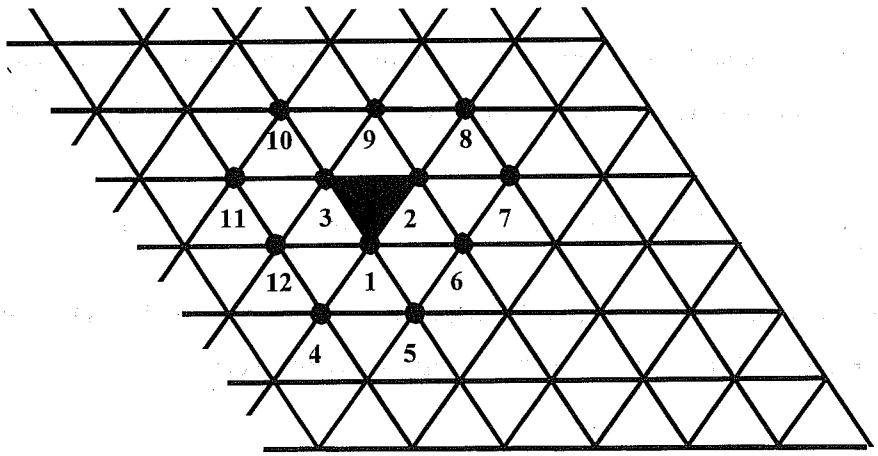

Figure 10 The twelve grid points involved in the biquadratic interpolation in the triangle P_0, P_1, P_2.

Monotonicity may be enforced by simply demanding that the interpolated value not be higher or lower than the values at the three corner points (P_0, P_1, P_2). In the same way, *positive definiteness* may be enforced by the condition that the interpolated value be greater than or equal to zero.

If the Courant numbers are restricted to values less than unity, it is fairly easy to determine which of the surrounding triangles contains the departure or midpoint of the trajectory. Without this restriction the search algorithm is more complicated and uses a binary search procedure to accelerate convergence.

2.4 Accuracy of the Gradient and Laplace Operators

Heikes and Randall (1995b) introduced the following function to test the accuracy of their finite-difference operators on the icosahedral-hexagonal grid

$$\beta_{m,n}(\lambda,\varphi)=a^2\cos^4(m\varphi)\cos(n\lambda) \tag{2.14}$$

where λ is the longitude, φ is the latitude, a is the radius of the earth, and m and n are integers set to 1 or 3. For different resolutions n_i of the grid the analytical solution x^{true} is compared to the finite-difference one x^{fd}, and some error norms are evaluated. The *one-norm* is defined by

$$\left\|x^{fd}-x^{true}\right\|_1=\frac{1}{A}\sum_{i=1}^{N}A_i\left|x_i^{fd}-x_i^{true}\right| \tag{2.15}$$

where the summation is over all N grid points of the icosahedral-hexagonal grid, A_i is the area of a particular hexagon (pentagon), and A is the area of the globe

$$A=\sum_{i=1}^{N}A_i \tag{2.16}$$

The *two-norm* is defined by

$$\left\|x^{fd}-x^{true}\right\|_2=\left[\frac{1}{A}\sum_{i=1}^{N}A_i\left(x_i^{fd}-x_i^{true}\right)^2\right]^{\frac{1}{2}} \tag{2.17}$$

and the *infinity norm* is defined by

$$\left\| x^{fd} - x^{true} \right\|_{\infty} = \max\left(\left| x_i^{fd} - x_i^{true} \right|, i = 1, N \right) \tag{2.18}$$

For the gradient operator, the norms of course include both components in the summations and in the evaluation of the maximum over the grid.

A finite-difference operator is said to be *consistent* if the infinity norm converges to zero for decreasing mesh sizes. Figs. 11 and 12 summarise the results for the GME gradient and Laplace operators. Both operators satisfy the consistency requirement. Their overall accuracy as characterised by their one- and two-norms is second order because the norms drop close to a factor of *4* when the resolution n_i is doubled. The GME operators constructed from the unaltered icosahedral-hexagonal grid thus display an accuracy similar to that of the operators derived by Heikes and Randall (1995 b, Fig. 4) on their twisted icosahedral-hexagonal grid where a special optimisation of the grid point distribution has been performed. Note that in Figs. 11 and 12, we include results not only for grids constructed with an initial bisection of the sides of the icosahedral triangles but an initial trisection as well. We also show results for grids with n_i values up to 768, corresponding to a horizontal resolution of about 10 km which is equivalent to T_L2000 for a spectral model.

It should be noted that the slope of the infinity norm changes from –2 to –1 for the Laplace operator. This occurs where errors due to local grid nonuniformity begin to dominate those due to the inherent inability of the finite grid to represent the function exactly. These maximum absolute errors captured by the infinity norm due to grid nonuniformity occur along arcs corresponding to the sides of the original 20 spherical triangles. The magnitude of these errors decreases by a factor of two as n_i is doubled while the area associated with such points also decreases by a factor of two. The fact that the one- and two-norms involve an area weighting factor explains why these norms maintain a slope close to –2 where the infinity norm switches to a slope of –1.

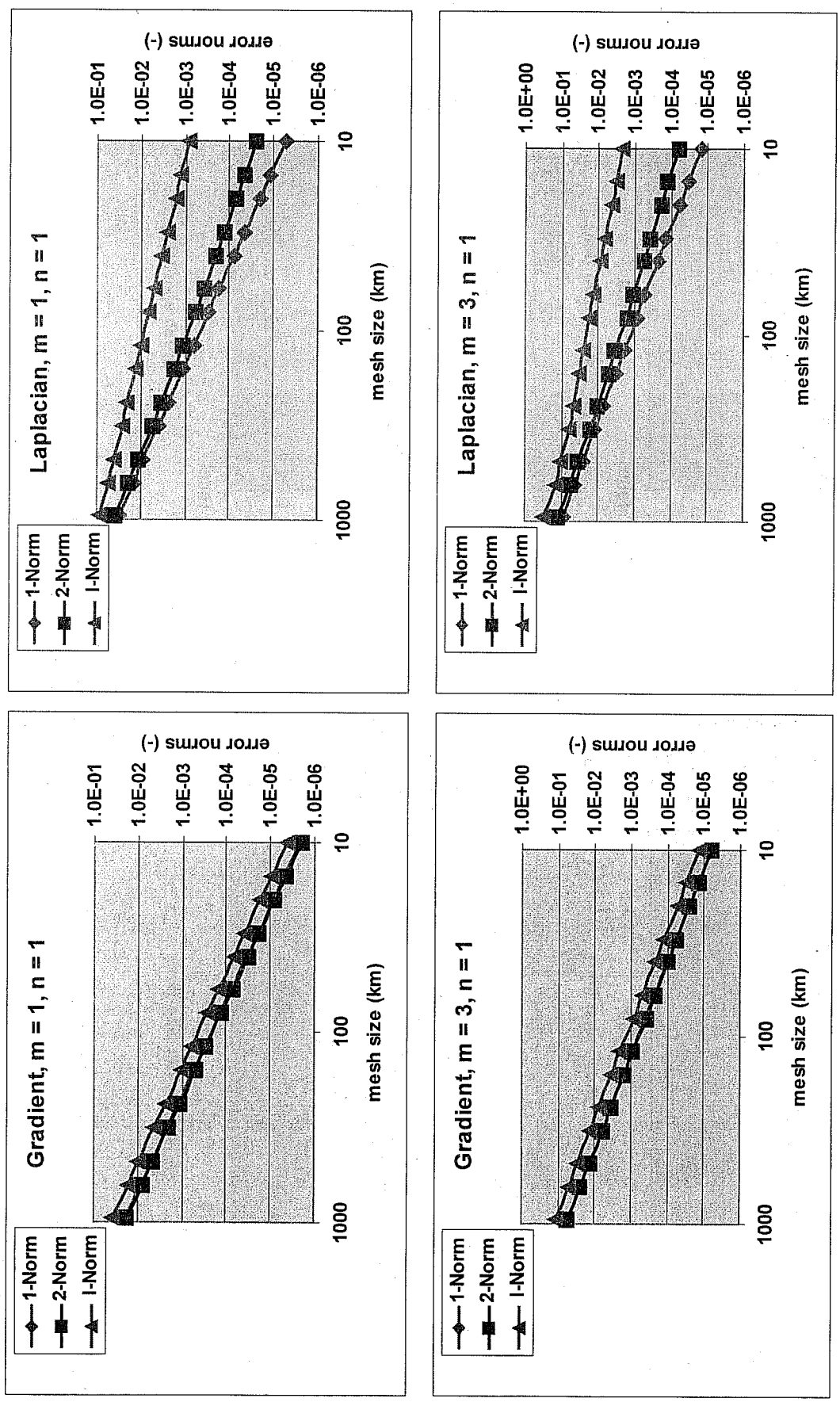

Figure 11 Error of the finite- difference **gradient** (left) and **Laplace** (right) operators as a function of mesh size for the test function proposed by *Heikes and Randall (1995b)* for m = 1, n = 1 and m = 3, n = 1.

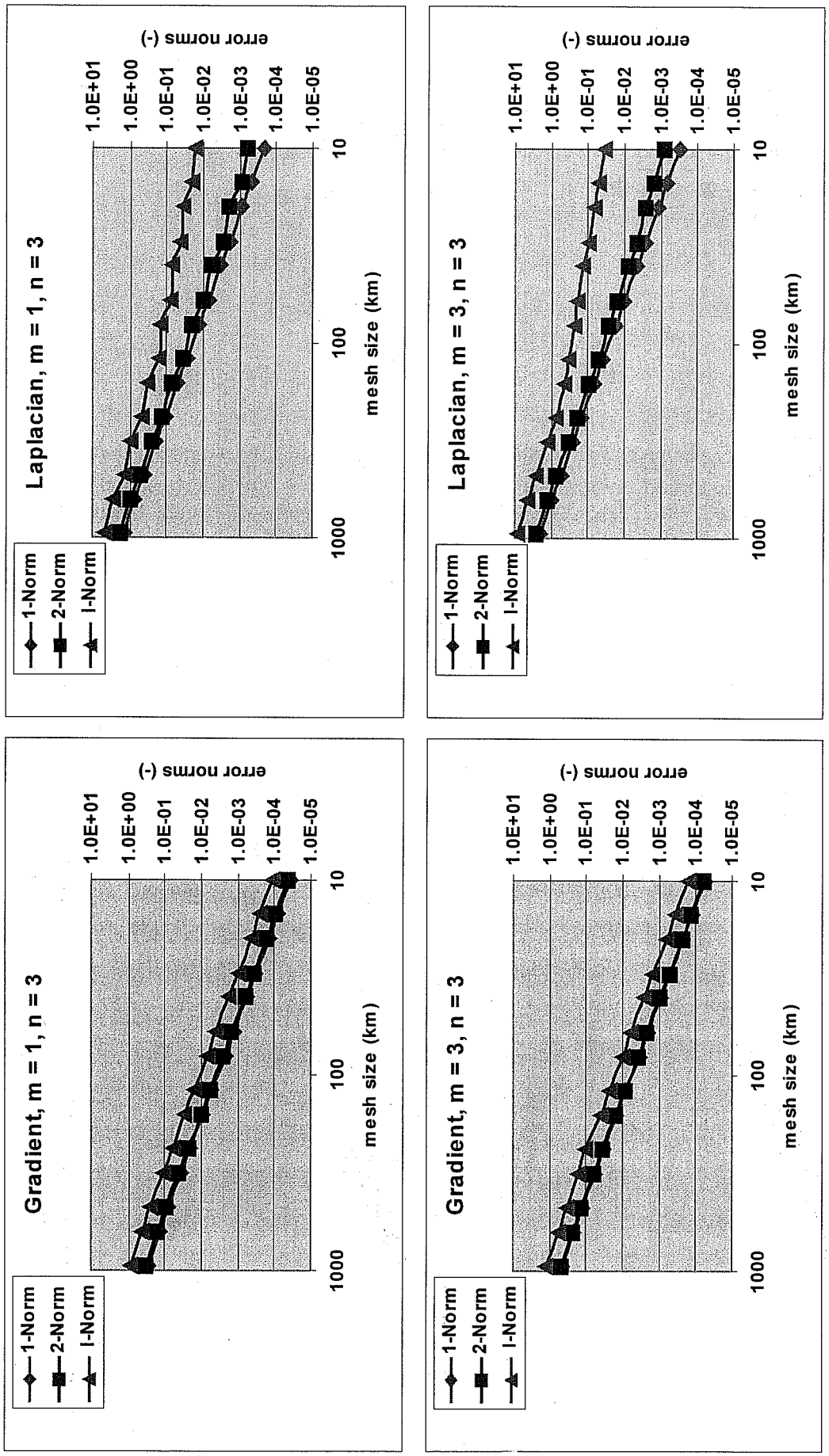

Figure 12 Error of the finite- difference **gradient** (left) and **Laplace** (right) operators as a function of mesh size for the test function proposed by *Heikes and Randall (1995b)* for m = 1, n = 3 and m = 3, n = 3.

3. THREE-DIMENSIONAL VERSION OF GME

3.1 Differential form of model equations

The prognostic equations of the three-dimensional version of the model are written in differential form for local spherical coordinates (η,χ) and a hybrid vertical coordinate ξ.

$$\frac{\partial u}{\partial t}-(\varsigma+f)v+\dot{\xi}\frac{\partial u}{\partial \xi}=-\frac{1}{a}\frac{\partial}{\partial \eta}(\Phi+K)-\frac{RT_v}{a}\frac{\partial}{\partial \eta}(\ln p)+\left(\frac{\partial u}{\partial t}\right)_{sub}-K_4\nabla^4 u \tag{3.1}$$

$$\frac{\partial v}{\partial t}+(\varsigma+f)u+\dot{\xi}\frac{\partial v}{\partial \xi}=-\frac{1}{a}\frac{\partial}{\partial \chi}(\Phi+K)-\frac{RT_v}{a}\frac{\partial}{\partial \chi}(\ln p)+\left(\frac{\partial v}{\partial t}\right)_{sub}-K_4\nabla^4 v \tag{3.2}$$

$$\frac{\partial T}{\partial t}+\frac{u}{a}\frac{\partial T}{\partial \eta}+\frac{v}{a}\frac{\partial T}{\partial \chi}+\dot{\xi}\frac{\partial T}{\partial \xi}=\frac{\alpha\omega}{c_p}+\frac{L_v}{c_p}C_{vc}+\left(\frac{\partial T}{\partial t}\right)_{sub}-K_4\nabla^4(T-T_{ref}) \tag{3.3}$$

$$\frac{\partial p_s}{\partial t}=-\frac{1}{a}\int_0^1\left\{\frac{\partial}{\partial \eta}\left(u\frac{\partial p}{\partial \xi}\right)+\frac{\partial}{\partial \chi}\left(v\frac{\partial p}{\partial \xi}\right)\right\}d\xi \tag{3.4}$$

$$\frac{\partial q_v}{\partial t}+\frac{u}{a}\frac{\partial q_v}{\partial \eta}+\frac{v}{a}\frac{\partial q_v}{\partial \chi}+\dot{\xi}\frac{\partial q_v}{\partial \xi}=-C_{vc}+\left(\frac{\partial q_v}{\partial t}\right)_{sub}-K_4\nabla^4 q_v \tag{3.5}$$

$$\frac{\partial q_c}{\partial t}+\frac{u}{a}\frac{\partial q_c}{\partial \eta}+\frac{v}{a}\frac{\partial q_c}{\partial \chi}+\dot{\xi}\frac{\partial q_c}{\partial \xi}=C_{vc}+\left(\frac{\partial q_c}{\partial t}\right)_{sub} \tag{3.6}$$

where

u,v are the zonal (meridional) wind components; T is the temperature; p_s is the surface pressure; q_v is the specific water vapour content and q_c is the specific cloud liquid water content; ζ is the vorticity and K the specific kinetic energy; p is the pressure and T_v is the virtual temperature; T_{ref} is a reference temperature depending only on height; C_{vc} is the condensation rate; $(..)_{sub}$ is the sub-grid scale tendency due to parameterized processes like radiation, convection or turbulence.

3.2 Numerical solution of the three-dimensional equation set

The shallow water test bed of the GME included a semi-Lagrangian and an Eulerian version of the code. The semi-Lagrangian version was restricted to Courant numbers less than 1. For larger Courant numbers the search algorithms and communication pattern become more complicated and were therefore not implemented in the short period of time available for the project. In the framework of the shallow water model both schemes produced very similar results but the Eulerian code was about 20% faster. Therefore, the *dry* part of the three-dimensional version of GME, i.e. the prognostic equations

for u, v, T, p_s, is solved by the semi-implicit Eulerian method, and only the two prognostic moisture equations (q_v, q_c) use semi-Lagrangian advection in the horizontal direction to allow for monotonicity and positive definiteness. In the vertical, the energy and angular momentum conserving finite-difference scheme of *Simmons and Burridge* (1981) is applied to all prognostic equations.

The semi-implicit treatment of gravity waves leads to a three-dimensional Helmholtz equation for the second temporal derivative of the divergence of the horizontal wind field. The eigenvectors of the vertical structure matrix are used to diagonalise this 3-d equation into *i3e* 2-d Helmholtz equations where *i3e* is the number of layers in the model. A split semi-implicit scheme (Burridge, 1975) is employed which solves only the Helmholtz equations corresponding to the external mode plus the first four internal ones. Currently, these five 2-d equations are solved by successive overrelaxation; about 20 iterations are needed to solve for the external mode, only 3 to 11 for the internal ones. A slight off-centering of the implicit terms is necessary to damp the gravity waves and to stabilise the solution. Part of the sub-grid scale tendencies are treated implicitly for stability reasons, too.

3.3 Physical Parameterizations

The simulation of diabatic processes in the icosahedral-hexagonal grid of the GME uses the same methods and procedures that are applied in any other NWP grid structure. However, the uniformity of the GME grid avoids unnecessary physics calculations in over-resolved high latitude zones that commonly occur in grids with polar singularities (e. g. regular latitude-longitude grids). In contrast to such grids, where the area represented by each grid node varies strongly with latitude, the distinction between resolved and unresolved atmospheric scales does not depend on the geographical position in the GME grid because the area of grid nodes varies by 20% at most. Unresolved atmospheric processes interact with the large-scale flow but contain also essential forecast information (e. g. cloudiness or precipitation) which can not be generated by the adiabatic part of the model. The simulation of such processes is the subject of a set of dedicated parameterization modules incorporated in the GME. The following physical phenomena are simulated by these modules

- radiative transfer of solar and thermal radiation in clear and cloudy atmospheres (*Ritter and Geleyn,* 1992); a full radiation step is performed every two hours at all grid points,
- grid-scale precipitation scheme including parameterized cloud microphysics (*Doms and Schättler,* 1997),
- deep and shallow convection based on a mass flux approach (*Tiedtke,* 1989),
- vertical turbulent fluxes (*Müller,* 1981); in the Prandtl-layer based on *Louis* (1979), for the boundary layer and the free atmosphere a diagnostic level-two scheme according to *Mellor and Yamada* (1974),
- sub-grid scale orographic effects (*Lott and Miller,* 1997),
- soil model (*Jacobsen and Heise,* 1982),

- cloudiness derived from specific cloud liquid water content, relative humidity, convective activity and stability.

For computational efficiency, some of the parameterization schemes (convection, turbulent fluxes, sub-grid scale orographic effects) are called only every fifth time step of the model.

With the exception of the sub-grid scale orographic effects scheme, which was adapted from the operational ECMWF forecast model, the parameterization modules have been used in the previous NWP system of the DWD, where they have undergone extensive testing and evaluation both in global and limited area model applications. In the framework of the GME the parameterization schemes needed some adjustments of the free parameters based on available validation and verification data.

3.4 External Parameters

Time-invariant grid point properties, such as mean orographic height, land-sea fraction, roughness length and soil type, are generally named *external parameters* and need to be computed for each grid element area based on high resolution supplementary data. Table 2 summarises the data sets used in the generation of external parameters for the GME.

Table 2 Description of data sets used in the generation of external parameters for the GME.

Dataset-	Source	Coverage	Resolution	Projection	Derived parameters
GLOBE	NOAA NGDC	global	30''	regular	h, stdh
GTOPO30	USGS	global	30''	regular	h, stdh
GLCC	USGS	global	~1 km	Goode homolosine	lf, z_0, root, plcov, lai
CORINE	ETC/LC	most European countries	250 m	Lambert azimuthal	lf, z_0, root, plcov, lai
DSM	FAO	global	5'	regular	soil type

CORINE: **CoORdination of INformation on the Environment**
DSM: **Digital Soil Map of the World**
ETC/LC: European Topic Centre on Land Cover
FAO: Food and Agricultural Organisation of UNO
GLCC : Global Land Cover Characterization
GLOBE: Global Land One-kilometer Base Elevation
USGS: United States Geological Survey

For each icosahedral-hexagonal grid element those high resolution raw data values which are associated with the corresponding geographical location are combined to form a grid area average; at the cur-

rent operational mesh size of 59.9 km, the average grid area is 3100 km^2. For some parameters the processing of the data also includes a conversion from basic information available, e. g. soil texture, to the model parameter required, e. g. soil type. In geographical regions where more than one raw data set is available for the same external parameter, a priority rule is applied in the processing based on a quality assessment of the raw data sets involved. E. g. for most grid elements in Europe land use dependent parameters are based on the CORINE information rather than on the lower resolution GLCC data set.

4. DATA ASSIMILATION SCHEME

4.1 Intermittent 4-d Data Assimilation Suite

The data assimilation scheme of the GME is based on a traditional intermittent 6-hourly analysis-forecast cycle. Analyses are performed at 00, 06, 12 and 18 UTC based on all observations valid in a 1.5 hour window around the analysis times. A 6-hour forecast of the GME provides the first guess to the analysis scheme.

4.2 Upper Air Analysis

Table 3 outlines the salient features of the upper air analysis. A multi-variate optimum interpolation (OI) scheme provides the analysis of the mass (surface pressure and geopotential) and wind (zonal and meridional wind components) fields simultaneously. The correlation functions employed until now are the ones of the former global spectral model (T106, L19) of the DWD; they will be replaced by functions properly describing the error statistics of the GME by the end of the year 2000. The upper air analysis is not performed on the icosahedral-hexagonal grid of the GME but on a regular latitude/longitude grid with a resolution 0.75° x 0.5° (480 x 361 grid points). Only the analysis increments are interpolated to the GME grid. In the near future, the analysis increments will be computed on the GME grid directly to avoid any smoothing due to the interpolation between model and analysis grids.

Table 3 Data assimilation and analysis of atmospheric fields for the GME

Method:	6 hourly intermittent data assimilation. Analyses at 00, 06, 12 and 18 UTC.
Main steps:	Analysis, initialization, forecast

	Mass and wind	**Humidity**
Method	3D multivariate optimal interpolation (OI) of deviations of observations from 6-h forecasts	3D univariate OI in the troposphere below 250 hPa. Constant specific humidity in the stratosphere
Analysed variables	Geopotential height, wind components, surface pressure	Relative humidity
Constraints	Analysed corrections locally approximately nondivergent and geostrophic	
First guess	6 hour model forecast	
Forecast error correlation	Product of a horizontal and a vertical part.	
	Horizontal model: Series of Besselfunctions Component length scale (middle latidutes): 400 km	$\mu_{ij} = e^{-\frac{1}{2}(r_{ij}/r_o)^2}$; $r_o = 300km$
	Vertical model: Empirical positive definite functions	
Observations	SYNOP, SHIP: Pressure. Winds from ships and from tropical landstations	Temperature and dewpoint. Total cloud amount and precipitation.
	TEMP, PILOT: Geopotential heights, winds (Only standard levels)	Temperature and dewpoint. Standard levels and significant levels up to 275 hPa
	SATOB: Winds. Not used over extratropical land areas	Upper troposphere humidity (UTH)
	SATEM: Thickness data at 250 km resolution. Not used over land below 100 hPa.	Precipitable water content for 3 layers
	AIREP, ASDAR: Winds	
Observation time window	± 1.5 hours	
Quality control	Comparison with first guess, comparison with OI analysis	
Realisation	Box method: Simultaneous analysis of a large number of data (up to 500) in large partial volumes of the atmosphere Analysis grid: (0.75° x 0.50°) geographical grid (480 x 361 grid points) Only analysis increments are interpolated to icosahedral-hexagonal model grid.	

4.3 Surface Analysis

The only surface fields analysed so far are the sea surface temperature (SST) and the snow depth. No analysis of soil temperatures and water contents is performed, but the 6-hour first guess fields of the GME are taken. Table 4 gives an overview of the surface analysis scheme. To avoid interpolation problems, the surface analysis is calculated on the icosahedral-hexagonal grid of the GME directly.

Table 4 Data assimilation and analysis of surface parameters for the GME

	Sea surface temperature (SST)	Snow depth
Analysis frequency	Daily at 00 UTC	6 hourly at 00, 06, 12 and 18 UTC
Method	Correction method. Increment calculation at grid points with local data selection. Influence radius: 450 km	Weighted average at grid points with local data selection. Influence radius: 330 km
Weights given to observations	a) Dependent on distance b) Dependent on age of observations	Dependent on horizontal and vertical displacement
Observations	SST-data from ships and buoys of the last 7 days	SYNOP snow depth observations. Snowfall data derived from SYNOP precipitation, temperature and weather observations of the last 6 hours
Quality control	Comparison with first guess and with nearby observations	Plausibility checks. Comparison with previous analysis
First guess	Previous analysis	Previous analysis
Adaption in data sparse areas	Blending with SST analysis from NCEP Washington	Use of snow depth forecast
Ice mask	Gridded sea ice analysis based on SSMI Satellite data from NOAA OMB. Interpolated into GME analysis grid	
Smoothing	2-D smoother is applied to the analysed field	

4.4 Incremental Digital Filtering Initialisation

Initialisation schemes have to remove noise from the forecast while causing acceptable small changes to the analysis and forecasts. Furthermore, if the initialisation achieves a better balance between humidity and dynamic fields, the spin-up problem can be alleviated. For the GME, the digital filtering initialisation (DFI) of Lynch (1997), involving a 3-h adiabatic backward integration and a 3-h diabatic forward one centered around the initial time, has been implemented. An incremental approach (IDFI) has been chosen which avoids unwanted smoothing of the first guess fields due to the DFI in regions without observations by applying the filter only to the analysis increments.

5. OPERATIONAL IMPLEMENTATION

5.1 Daily Schedule of Analyses and Forecasts

Since 1st December 1999 the GME is the operational global NWP model of the DWD and provides the meteorological data base for many follow-up products and systems. The GME and its data assimilation scheme are implemented on the Cray T3E1200 of the DWD; the GRIB (*Gri*dded *B*inary) code analysis and forecast data are stored in huge ORACLE data bases on an SGI Origin cluster.

The operational schedule is structured by *data assimilation* steps every six hours, i. e. for 00, 06, 12 and 18 UTC with a data cut-off between 7 to 12 hours. An *early run* with a data cut-off of 2h 14min and forecasts up to 78 hours allows early numerical guidance, and provides lateral boundary conditions for the nonhydrostatic regional model LM (7 km mesh size, 35 layers) of the DWD as well as the regional models of ten other NMS (see 5.3). The early runs are based on 00, 12 and 18 UTC analyses and use 13 x 13 processors. To complete the 78-h forecast takes about 50 minutes wallclock time. The *main run* with a data cut-off of 3h 30min and forecasts up to 174 hours is based on 00 and 12 UTC analyses. With 15 x 15 processors the whole 174-h forecast takes 1h 35min.

5.2 Available Products

GME data are mostly stored on the icosahedral-hexagonal grid (Arakawa-A, 163842 grid points, 31 hybrid layers). More than 80% (11 GByte) of the data of a 174-h forecast are given in this spatial representation. Software is available to extract the GME forecast at single grid points anywhere on the globe to derive meteographs. To ease the data visualisation and as an interface to applications like wave modelling, selected forecast fields are interpolated horizontally from the icosahedral-hexagonal grid to a regular latitude/longitude one (0.75° x 0.75°). Moreover, some multi-level fields are interpolated vertically from the 31 model layers to selected pressure levels.

5.3 GME Data as Lateral Boundary Conditions at other NMS

Forecast data from the *early run* of the GME are sent via the internet to other national meteorological services (NMS). These data serve as initial and lateral boundary conditions for regional NWP models, which are based on either the high-resolution regional model (HRM) of the DWD or the nonhydrostatic LM. Only those GME grid points which cover the domain of interest of the NMS in question are transmitted to reduce the amount of data. Because of this, real-time distributed computing has been realised, where the GME at the DWD and the regional models at the NMSs run in parallel and the internet is used for the transfer of the lateral boundary data. Currently, the following ten NMSs are receiving the GME data twice daily based on 00 and 12 UTC data out to 48 (78) hours at 3-hourly (for some even at hourly) intervals

- Brazil (Directorate of Hydrography and Navigation),
- Brazil (Instituto Nacional de Meteorologia),
- China (Guangzhou Regional Meteorological Centre),
- Greece (National Meteorological and Hydrological Service),
- Israel (Israel Meteorological Service),
- Italy (Regional Service SMR-ARPA),

- Oman (National Meteorological Service, DGCAM),
- Poland (National Meteorological Service, IMGW),
- Romania (National Meteorological and Hydrological Service),
- Switzerland (National Meteorological Institute).

Most of the regional models running at the NMSs have resolutions between 30 and 7 km; they are able to add valuable details to the GME forecast because the topographical forcing generally modifies the larger scale flow provided by the GME.

6. SOME RESULTS OF DIAGNOSTICS AND VERIFICATION

6.1 Systematic Trends in 60-d Forecasts

To detect systematic trends in the GME forecasts a 60-d (=1440 h) run has been performed at the operational resolution of 60 km and 31 layers. The forecast was initialised on 15 Dec. 1999 at 00 UTC and used constant sea surface temperature. Global diagnostics were produced each day to monitor the model evolution. The results are summarised in Fig. 13. No obvious trends are visible at first glance. The volume average of the kinetic energy (Fig. 13, top left) varies slowly between 150 and 175 m^2/s^2 whereas the maximum wind speed (usually found at the top level, i. e. at 10 hPa) fluctuates on a much shorter time scale between 80 and 140 m/s. Although the mass (Fig. 13, top right) is not formally conserved, the mean deviation from the initial state never exceeds 0.14 hPa. The hydrological quantities (Fig. 13, bottom) seem to be balanced rather well throughout the 60-d period; only a slight tendency is visible to shift the precipitation from the convective to the grid-scale regime.

6.2 Verification of Precipitation Forecasts

The Global Precipitation Climatology Centre (GPCC) provides an objective analysis of monthly precipitation. This analysis is based on measurements at about 6000 surface stations over land and estimated amounts derived from brightness temperatures of geostationary satellites over the oceans. The spatial resolution of the combined product is 2.5° x 2.5° (Fig. 14, bottom). For February 2000, the precipitation forecasts of the GME for the 24-h period 06 to 30 hours have been accumulated for each day to derive a monthly value (Fig. 14, top). There is close correspondence between observation and simulation of the main features like the precipitation extremes at the ITCZ and the storm tracks of both hemispheres. Even the heavy flooding which hit Mozambique in Februray, has been forecasted by the GME rather well. Concerning the distribution over the continents, the model is able to simulate the topographical modification of the precipitation field in more detail than can be depicted by the GPCC analysis due to the coarse resolution of the observing network.

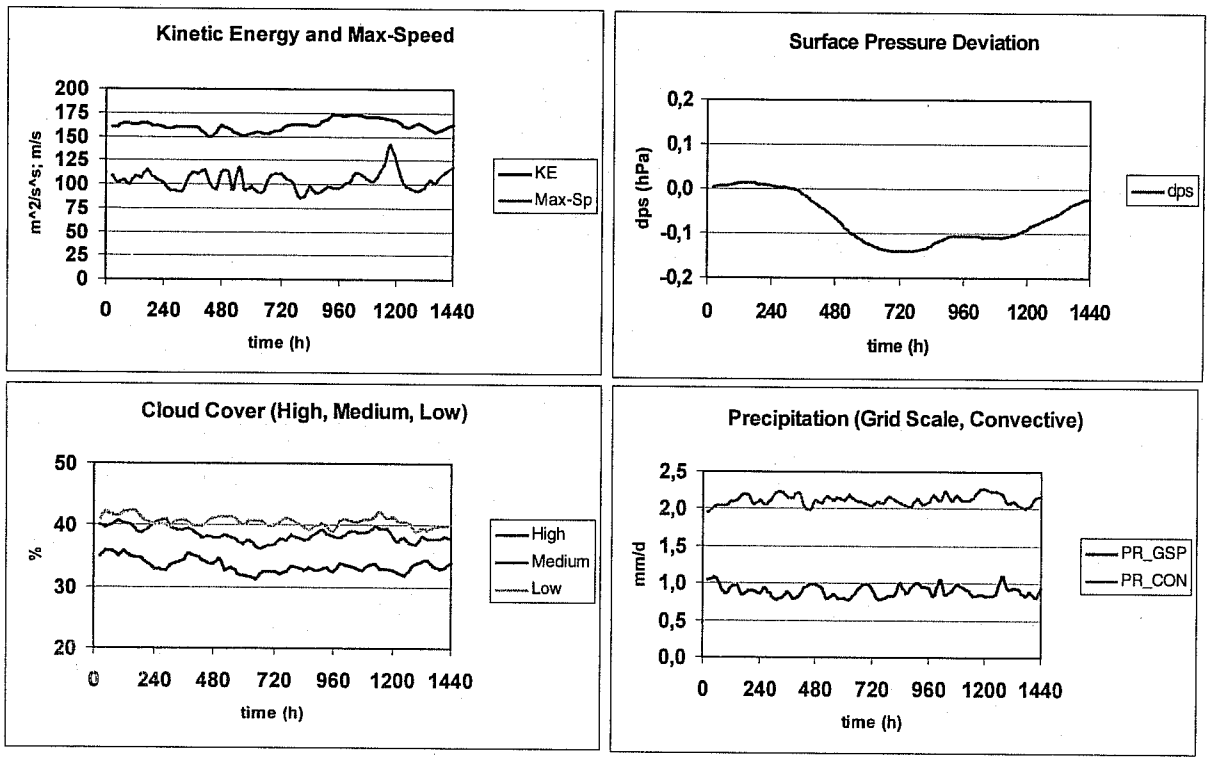

Figure 13 Diagnostic evaluation of a 60-d run of the GME initialised on 15 Dec. 1999 at 00 UTC.

6.3 Kinetic Energy Spectra

Based on the horizontal wind components at the icosahedral-hexagonal grid points of the GME the kinetic energy spectrum has been computed by replacing the integrals by summations over the grid elements. At the operational resolution $n_i = 128$ with 163842 grid points, a triangular truncation of up to T340 is possible. Fig. 15 shows the resulting spectrum of the eddy kinetic energy (after summation over the zonal index m for $m > 0$) at 250 hPa on 25 May 2000 at 00 UTC. The full spectrum is shown on the left, the higher end between wave numbers 150 to 340 is shown to the right. No "wave number 5 problem" can be detected in the GME spectrum. For comparison, the spectrum of the ECMWF model (T_L319, 60 layers) is depicted, too. Both models show close agreement up to wave number 100, especially the n^{-3} drop of energy in the wave number range between $n = 10$ to $n = 100$. At higher wave numbers, the GME spectrum falls off at a rate close to $n^{-5/3}$ whereas the ECMWF one drops off at a much higher rate indicating a stronger (and more effective) horizontal diffusion of the model. Integrated over the full spectrum, both models have almost the same level of eddy kinetic energy (for the GME: 133.8 m^2/s^2 and the ECMWF model: 135.8 m^2/s^2).

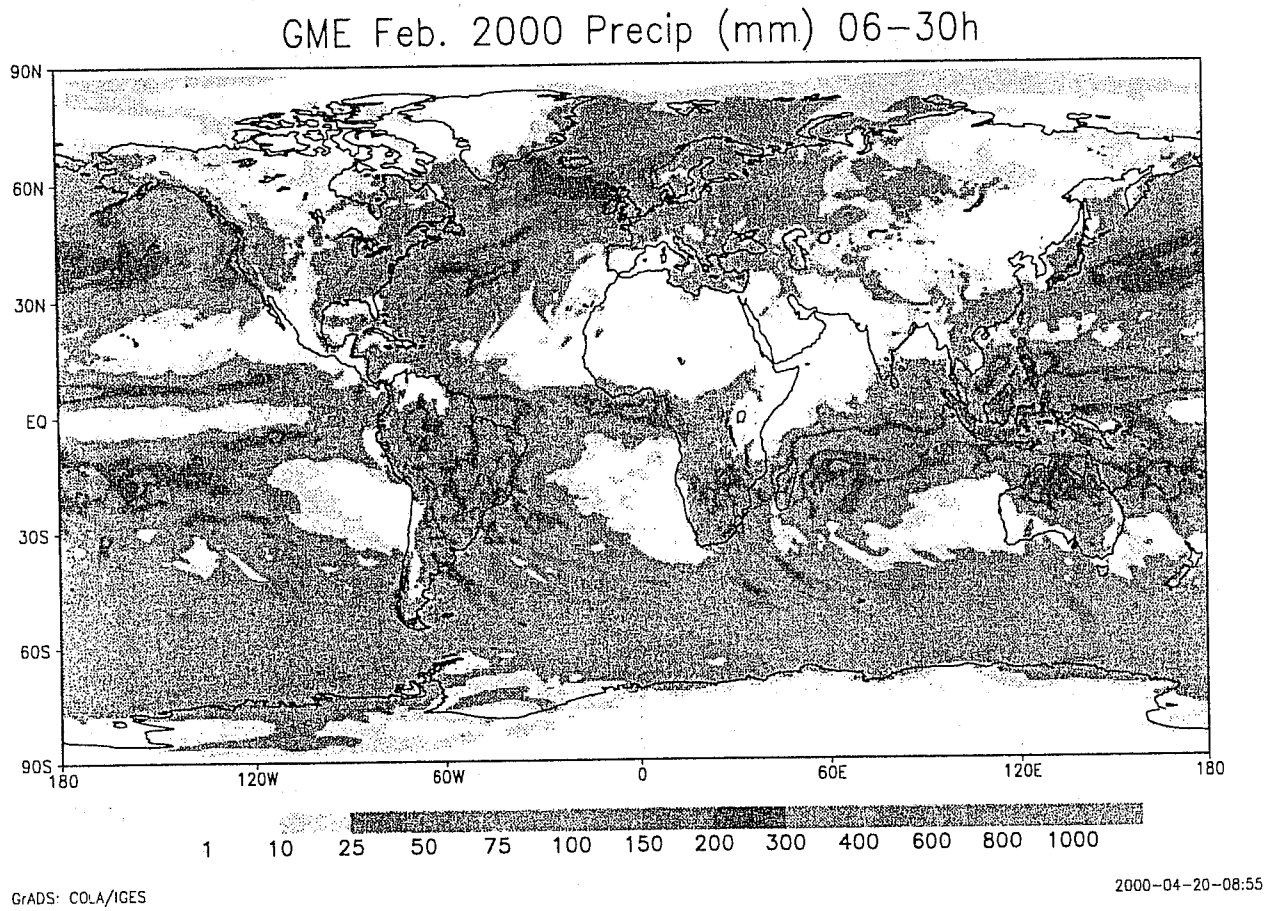

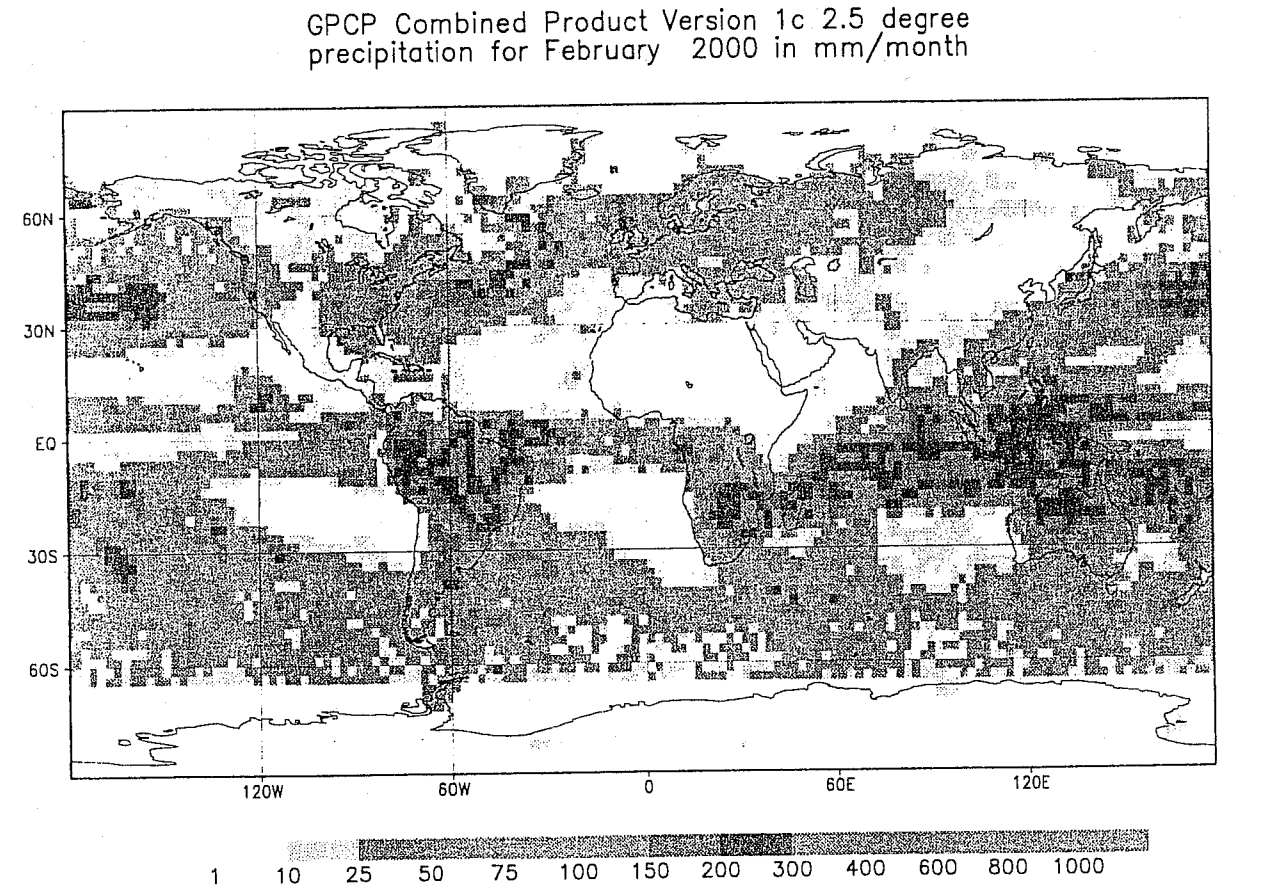

Figure 14 Monthly precipitation (mm) for February 2000. Top: GME forecasts, time range: 06 to 30 hours. Bottom: Analysis of the GPCC, combined product.

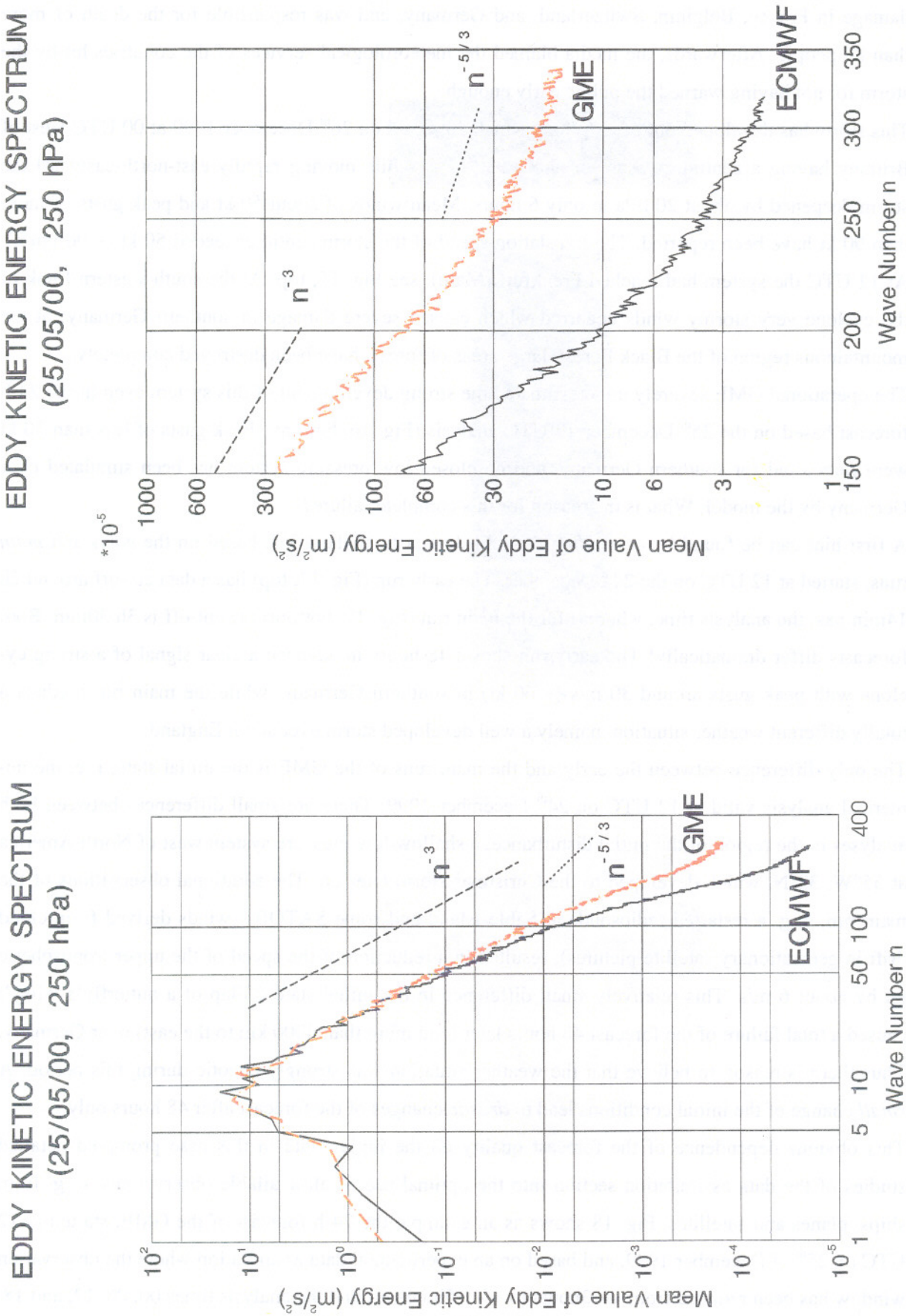

Figure 15 Eddy kinetic energy spectrum of the GME and the ECMWF model at 250 hPa.

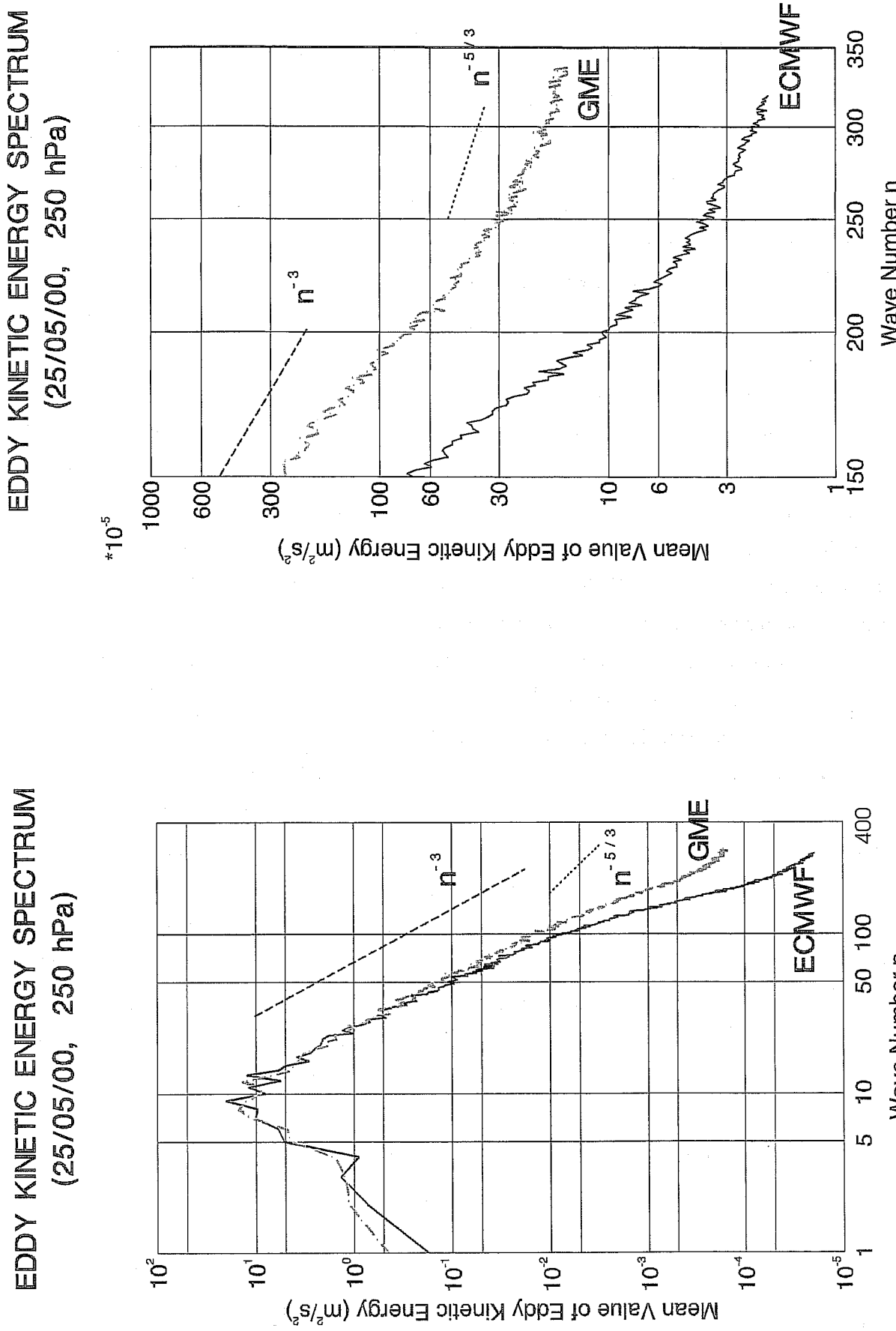

Figure 15 Eddy kinetic energy spectrum of the GME and the ECMWF model at 250 hPa.

6.4 Christmas 1999 Storm in France and Germany or "The Flap of a Butterfly's Wing"

On December 25, 1999, a strong winter storm with peak gusts of more than 200 km/h caused huge damage in France, Belgium, Switzerland, and Germany, and was responsible for the death of more than 80 people. Afterwards, the media blamed the meteorological services of the countries hit by the storm for not having warned the public early enough.

This storm has developed out of a cyclone which appeared on 26th December 1999 at 00 UTC west of Brittany having a central pressure of about 980 hPa. While moving rapidly east-north-eastward the storm deepened by about 20 hPa in only 6 hours. Mean winds of about 50 kt and peak gusts of more than 90 kt have been reported. The translation speed of the storm centre exceeded 50 kt (~ 90 km/h). At 12 UTC the system had reached Frankfurt (Main), see Fig. 16, top. At the south-western flank of the cyclone very stormy winds occurred which caused severe damage in southern Germany; at the mountainous region of the Black Forest, large areas of forests have been destroyed completely.

The operational GME severely underestimated the strong development of this system even in the 24-h forecast based on the 25th December 12 UTC analysis (Fig. 16, bottom). Peak gusts of less than 30 kt were forecasted for southern Germany, and no closed low pressure system has been simulated over Germany by the model. What is the reason for this complete failure?

A first hint can be found by comparing the 48-h forecasts of the GME based on the *early* and *main* runs, started at 12 UTC on the 24th December. The early run (Fig. 17, top) has a data cut-off around 2h 14min past the analysis time, whereas for the main run (Fig. 17, bottom) the cut-off is 3h 30min. Both forecasts differ dramatically! The early run shows 48 hours in advance a clear signal of a strong cyclone with peak gusts around 30 m/s (~ 60 kt) in southern Germany, while the main run predicts a totally different weather situation, namely a well developed storm over south England.

The only difference between the early and the main runs of the GME is the initial state, i. e. the numerical analysis valid at 12 UTC on 24th December 1999. There are small differences between both analyses in the region of the initial disturbance, a shallow low pressure system west of North America at 55°W, 38°N, which developed to the Christmas storm later on. The additional observations of the main run, e. g. a restarted radiosonde at Sable Island and some SATOBs (winds derived from cloud drift in geostationary satellite pictures), resulted in a reduction of the speed of the upper tropospheric jet by about 6 m/s. This relatively small difference in the initial state ("Flap of a butterfly's wing") caused a total failure of the forecast 48 hours later (and more than 4000 km to the east) over Germany. Thus there is reason to believe that the weather situation was strongly chaotic during this period. A *small* change of the initial conditions lead to *drastic* changes of the forecast after 48 hours only.

This obvious dependence of the forecast quality on the initial state in this case prompted detailed studies of the data assimilation section into the optimal use of all available observations, e. g. from ships, planes and satellites. Fig. 18 shows as an example the 24-h forecast of the GME, started at 12 UTC on 25th of December 1999, and based on an experimental data assimilation where the observation window has been reduced from +/- 3hours to +/- 1.5hours around the analysis times 00, 06, 12, and 18

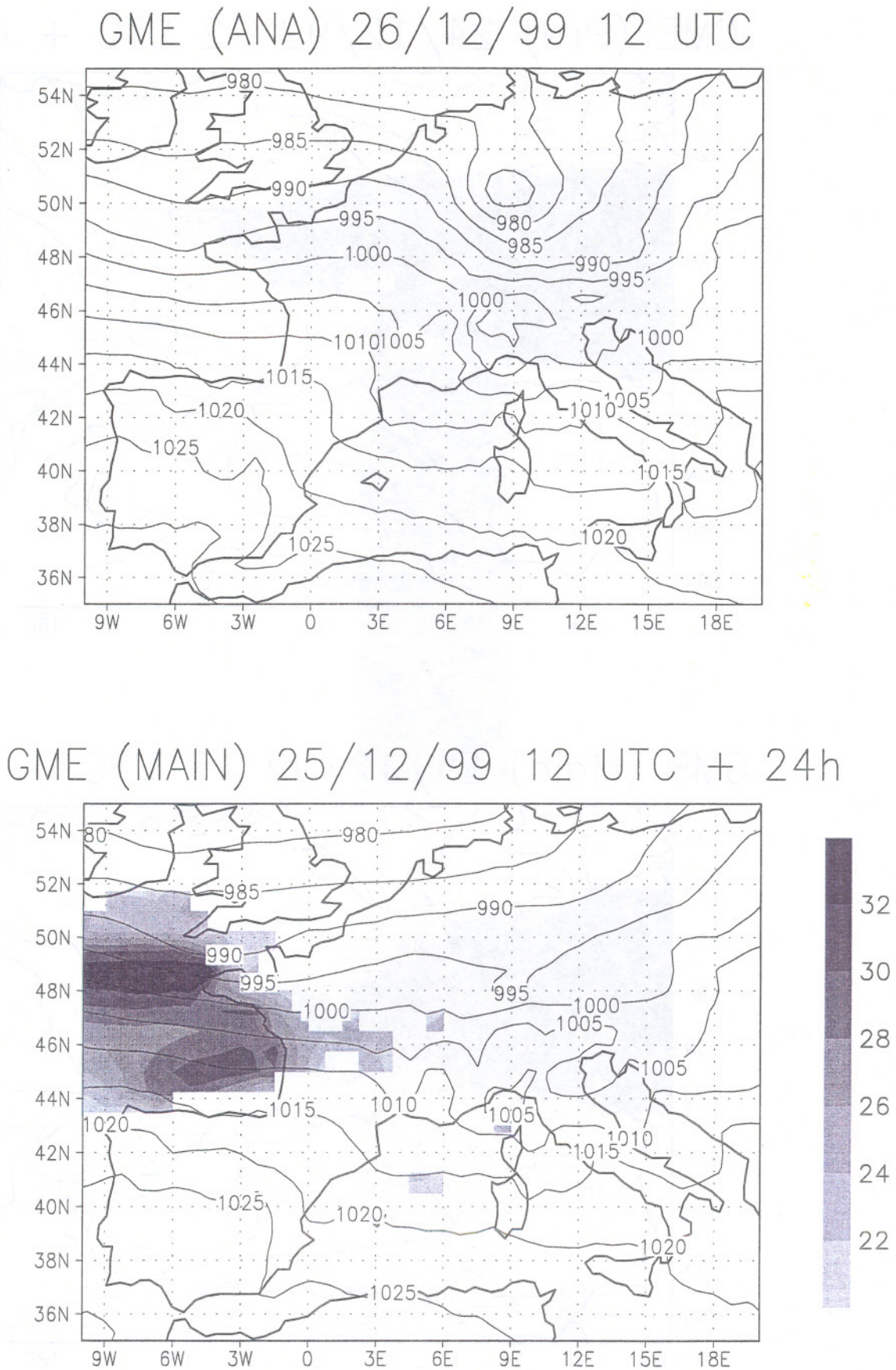

Figure 16 Top: GME analysis of mean sea level pressure (hPa) at 12 UTC on 26 Dec. 1999. Bottom: 24-h GME forecast of mean sea level pressure (hPa) and maximum wind speed (m/s, shading) valid at 12 UTC on 26 Dec. 1999.

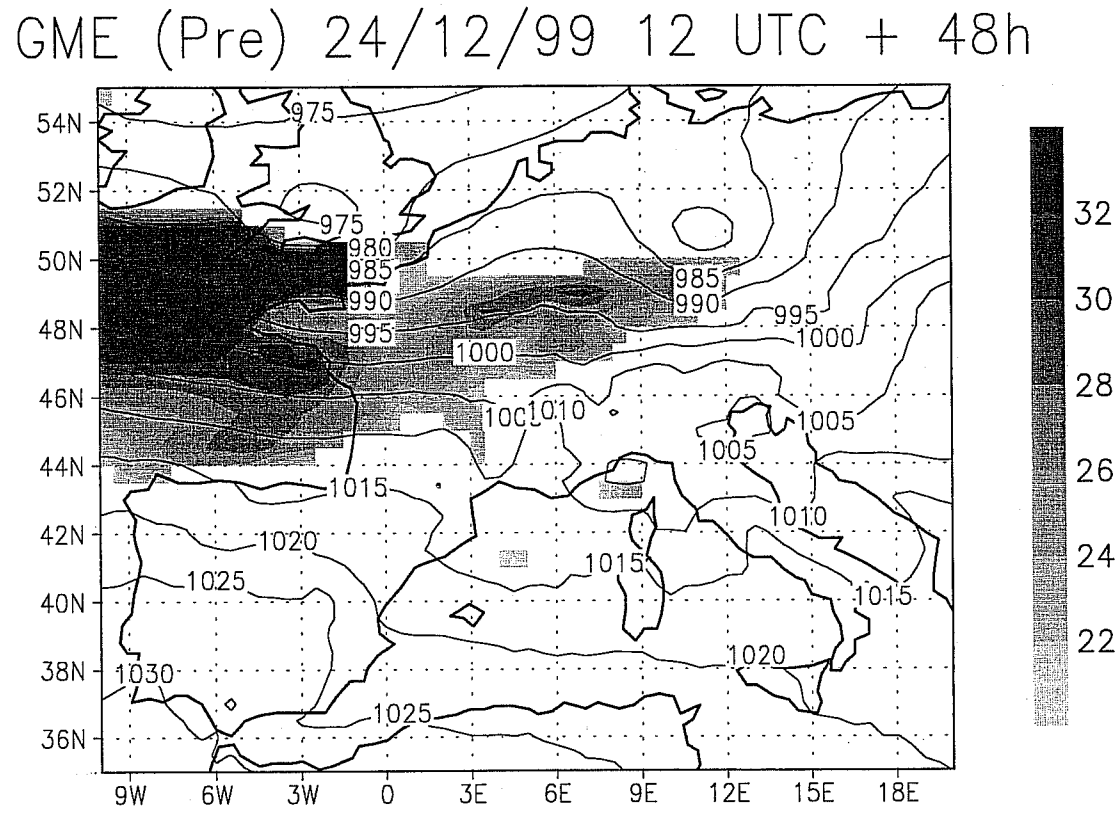

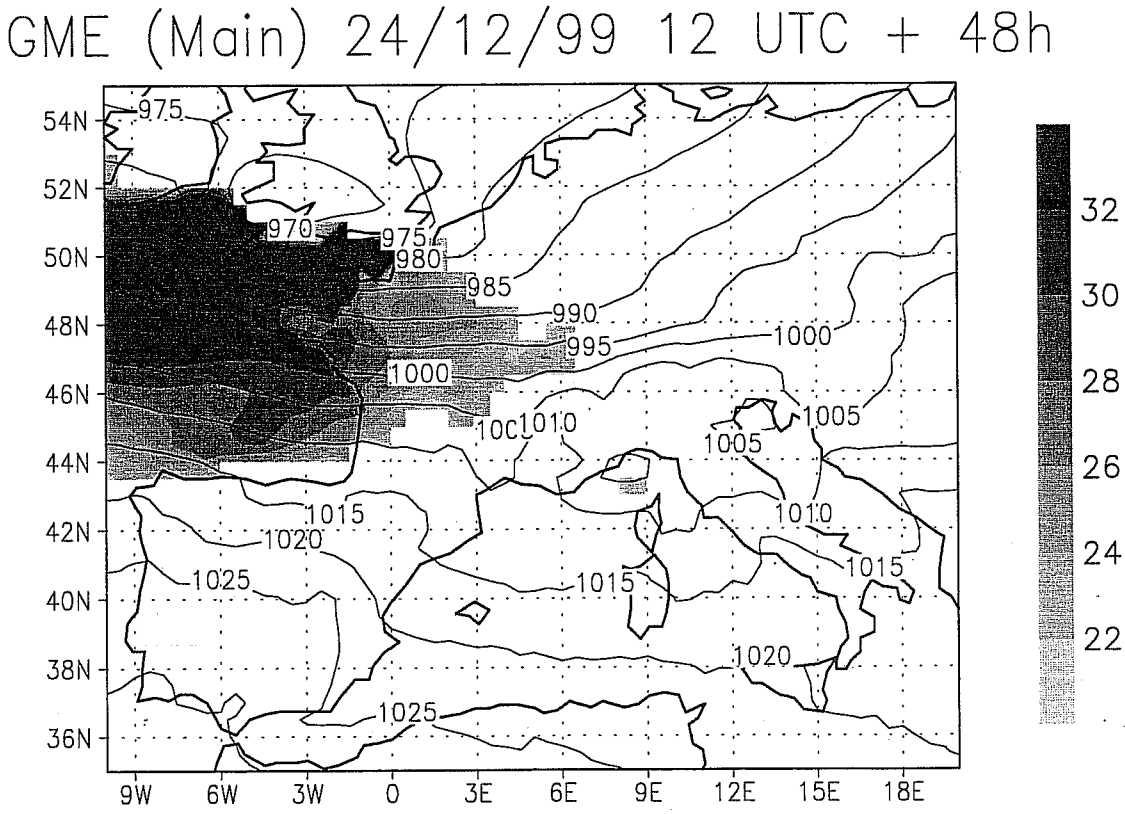

Figure 17 48-h GME forecasts of mean sea level pressure (hPa) and maximum wind speed (m/s, shading) valid at 12 UTC on 26 Dec. 1999.
Top: Early run (data cut off: 2h 14min). Bottom: Main run (3h 30min).

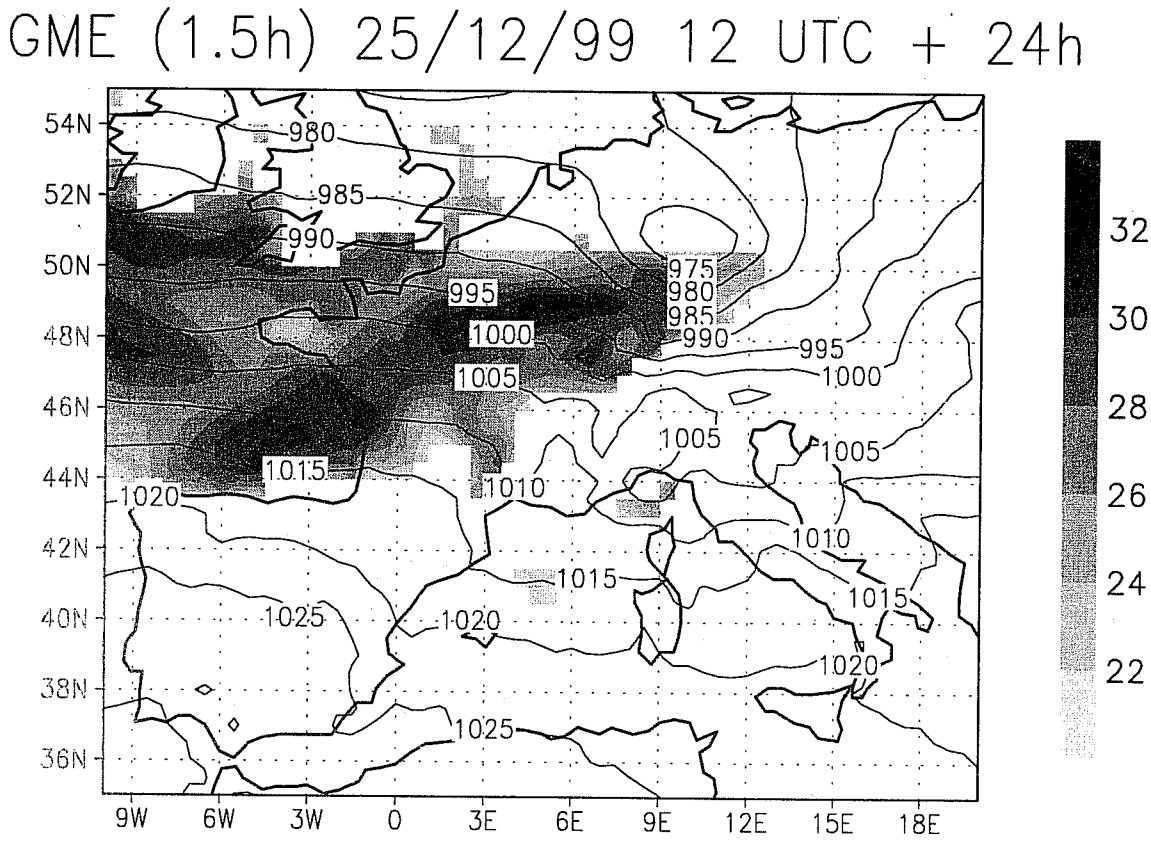

Figure 18 24-h GME forecast (based on 1.5 h observation window for the analysis) of mean sea level pressure (hPa) and maximum wind speed (m/s, shading) valid at 12 UTC on 26 Dec. 1999.

UTC. This reduction avoids the "smearing out" of the information in rapidly changing flow situations. With a mesh size of 60 km, the GME is of course not able to simulate the rapid deepening (and filling) of the storm over France in all mesoscale details, but the comparison (Fig. 19) between the observed and simulated temporal evolution of the surface pressure at Paris (Orly Airport) reveals reasonable correspondence. Even the nonhydrostatic high resolution regional numerical weather prediction model LM with its 7-km grid mesh is unable to catch the rapid deepening and filling of this storm in full detail.

The reduction of the observation window improved the forecast quality of the GME not only in this case, but for the second French storm (28 Dec. 1999) as well as for the Danish storm (3 Dec. 1999). Since May 2000, the shortened observation window is applied operationally, too.

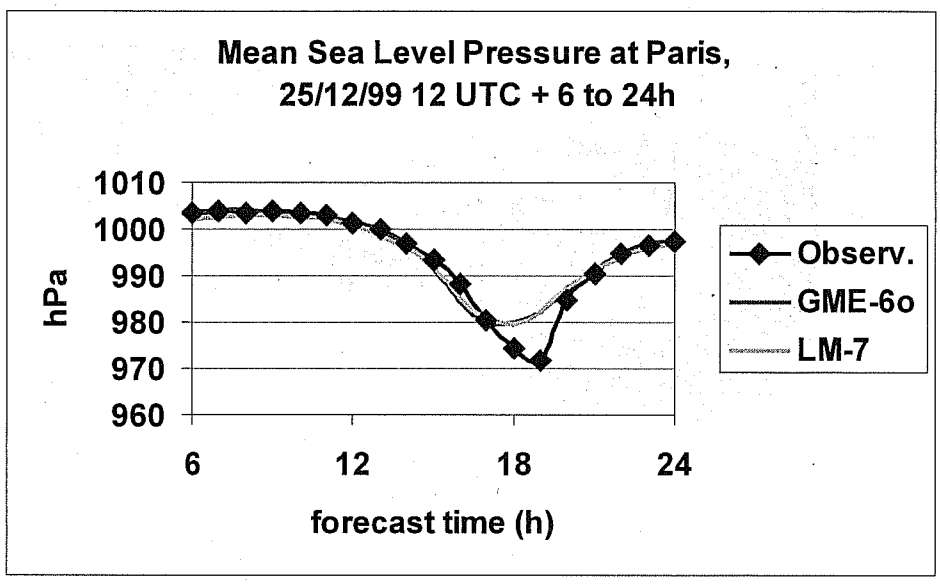

Figure 19 Temporal evolution of the surface pressure at Paris Orly between 25 Dec. 1999 18 UTC and 26 Dec.1999 12 UTC. Observed and predicted by the GME and the Lokal-Modell (LM, 7-km mesh).

7. HIGH RESOLUTION TESTS

7.1 Parallelization on MPP Systems

Since the design of the GME included a domain decomposition from the beginning, it took only three months to parallelise the program using MPI (Message Passing Interface) for message passing. The code is written in standard FORTRAN 90 and fully portable. For the two-dimensional domain decomposition (Fig. 20) the $(ni+1)^2$ grid points of each diamond are divided among *n1 x n2* processing elements (PEs). Thus each PE computes the forecast in a subdomain of *all ten* diamonds. This approach improves the chance to achieve a better load balancing for the physical parameterizations, e.g. between day/night, land/sea or rain/no rain. For example, on 13 x 13 PEs of a Cray T3E1200 the physical parameterizations for a 24-h real data forecast consume between 250s and 316s of wallclock time; the average time is 279s. In the current version of GME, each computational subdomain has a *halo* of just two rows and columns of grid points which have to be exchanged via MPI with those PEs which compute the forecast in the neighbouring subdomains. There are only seven synchronisation points during one complete forecast step. It should be noted that good load balancing requires that all processors have nearly the same workload; thus the difference between the mean and the maximum number of grid points in the computational subdomains should be small.

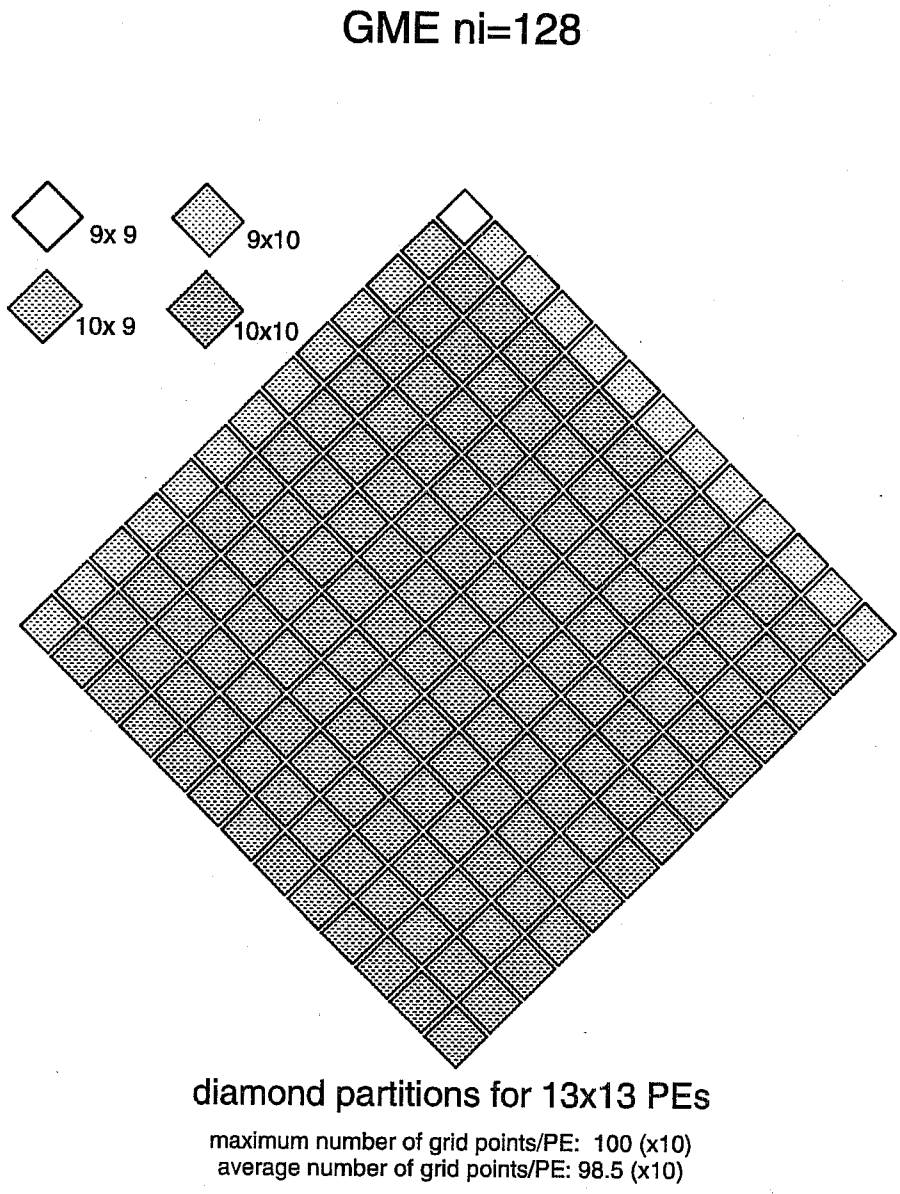

Figure 20 Two-dimensional domain decomposition of a diamond of the GME for 13 x 13 PEs.

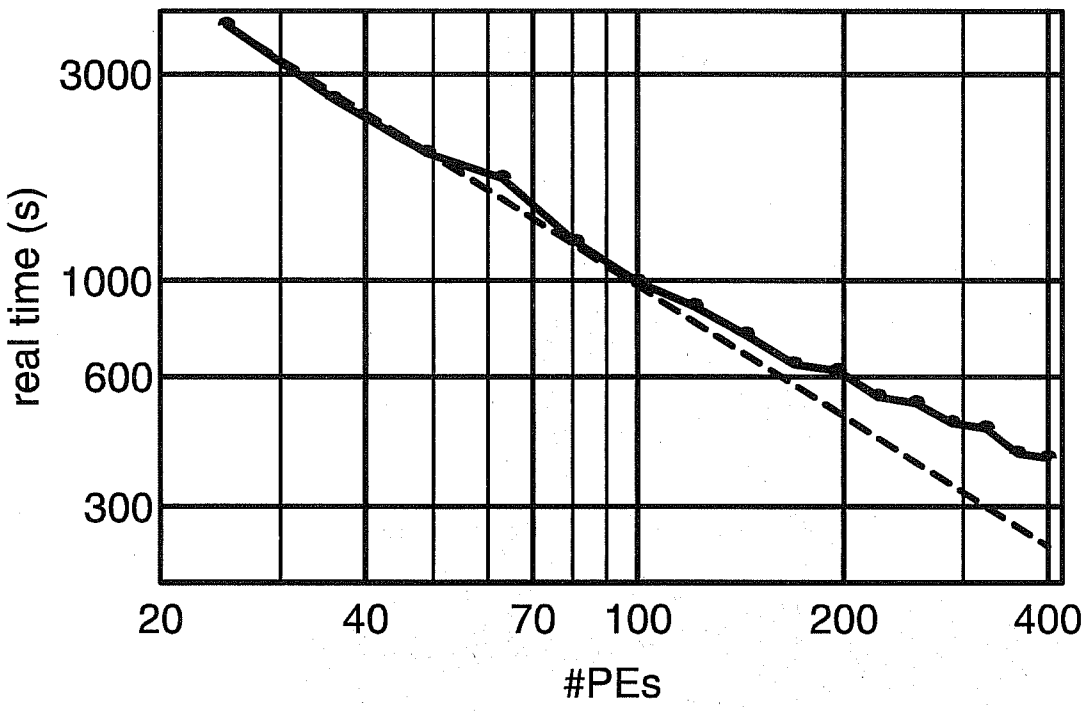

Figure 21 Speed-up of GME (60 km, 31 layers) on a Cray T3E1200 for a 24-h real data forecast without postprocessing.

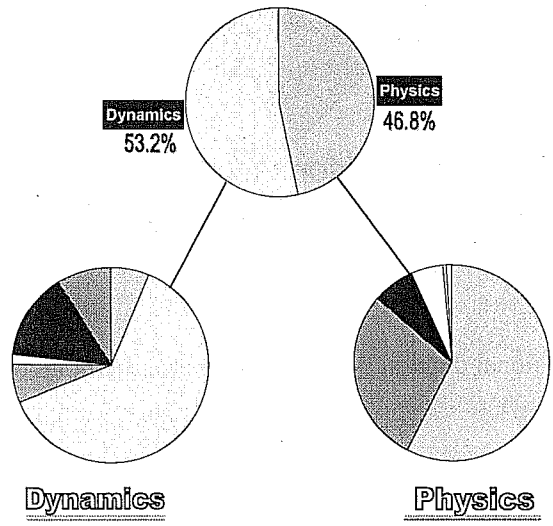

SL trajectories	6.3 %	Radiation	57.5 %
Explizit step	62.2 %	Grid-scale precip.	29.0 %
SI, r. h. s.	6.5 %	Convection	6.7 %
SI, SOR	1.8 %	Turbulence	5.4 %
SI, add	14.2 %	SSO	0.7 %
Geopot./ condens.	9.0 %	Soil	0.7 %

Computational cost of different parts of the GME (unit: percentage of total cost) for a 24-h forecast on a Cray T3E. ni= 128, $\Delta \sim 60$ km, 31 layers, $\Delta t = 240$s, $\Delta t_{Rad} = 2$h.

Figure 22 Cost of the different parts of GME (60 km, 31 layers) on a Cray T3E1200 for a 24-h real data forecast without postprocessing. 13 x 13 PEs have been used.

7.2 Performance of the GME on the Cray T3E

The GME has been ported successfully to several parallel platforms based on vector or RISC processors. However, the effort devoted to optimising the GME code for different computer systems has been rather limited so far, thus there is surely quite a lot of potential for improvement of the performance of the model.

Fig. 21 shows the speed-up of the GME (60 km mesh size, 31 layers) on a Cray T3E1200 for a 24-h real data forecast without postprocessing. Between 5 x 5 and 13 x 13 PEs an almost linear speed-up can be realised. About 60 PEs are necessary to perform a 24-h forecast in less than 30 minutes.

The distribution of the cost of the different parts of GME expressed as percentage of the total number of floating point operations on a Cray T3E1200 is highlighted in Fig. 22.

7.3 Global Forecasts at Resolutions Ranging from 160 Down to 15 km

Current global models of major NWP centres employ horizontal mesh sizes of about 60 km and require about 5×10^{12} floating point operations (Flop) for a 24-h forecast. A few years from now, global models with mesh sizes in the range between 10 to 20 km will be feasible.
On the Fujitsu VPP5000 of the ECMWF the GME has been tested for the mesh sizes 160, 120, 80, 60, 40, 30, 20 and 15 km. Fig. 23 compares the depiction of the Alps at the different resolutions; the peak height increases from 1596 m at 160 km to more than 3000 m at 15 km.
The initial state of the test runs has been derived from a rather coarse resolution analysis (T106L19, i.e. a mesh size of about 120 km, 19 layers) by interpolation to the GME grids. Thus these runs cannot show the full potential of high resolution global modelling because the data assimilation part is missing. Here, the main goal is to test the behaviour of the GME at different resolutions from the computing point of view. The case chosen is the Christmas storm (see section 6.4) with the initial date 25 Dec. 1999 12 UTC. A 24-h forecast with postprocessing only at 18 and 24 hours has been performed for each resolution. The results are summarised in Table 5 and Fig. 24.

Table 5 Some characteristic numbers of the Global Model GME at different horizontal resolutions based on measurements on the Fujitsu VPP5000 at the ECMWF. The number (i3e) of layers is set to 31 for all resolutions. n_i is the resolution of the icosahedral grid, Δ is the mesh size, N is the number of grid points/layer, Δt is the time step, HWM is the high water mark of memory used by the GME.

n_i	Δ (km)	N/layer	Δt (s)	HWM (MW)	Cost (10^{12} Flop) of 24-h forecast	Speed (Gflop/s) for 24-h in 900s
48	160	23.042	640	112	0.43	0.48
64	120	40.962	480	144	0.85	0.94
96	80	92.162	320	224	2.43	2.70
128	60	163.842	240	336	5.23	5.82
192	40	368.642	160	752	15.97	17.74
256	30	655.362	120	1.408	36.52	40.58
384	20	1.474.562	80	2.752	111.79	124.22
512	15	2.621.442	60	4.864	259.29	288.10
768	10	5.898.242	40	10.000*	800.00*	900.00*

* estimated

$$\mathbf{Cost_{24h}\ (Flop) \sim [\ 24 * 3600s/\Delta t * 2.1 + n_{Rad} * 21.8) * 10^3 * (n_i + 1)^2 * 10 * i3e}$$

A halving of the mesh size Δ, i. e. a doubling of the resolution, is normally associated with a factor of *eight* increase of the computational cost of the forecast. This is due to the fact that the time step of the model usually has to be halved as well due to the CFL criterion. Looking at the results presented in Table 5, in practise the factor is much less for the GME, e. g. for a reduction of the mesh size from 160 km to 80 km, the factor is only *5.65*. This smaller increase in the computational work load is due to processes which do not depend on the time step directly, namely the parameterization of radiation and postprocessing. A full radiation step is performed every *two* hours at each grid point of the GME. At the resolution of 160 km, the radiation takes about 40% of the total computational cost, but at high resolutions like 20 km this portion is down to 11%. Moreover, on vector machines like the Fujitsu VPP5000 the wallclock time of the model run may not increase as much as expected because of the greater vector length at higher resolutions. E. g. for the GME, the speed on each processor increases from 0.9 GFlops at 160 km (with an average vector length of 62 elements) to 2.3 GFlops at 20 km (with an average vector length of 348 elements).

From the meteorological point of view, the surface pressure forecasts at the different mesh sizes (Fig. 24, isolines) differ only in details for resolutions beyond 120 km. For coarser resolutions, the storm moves too slowly to the east. On the other hand, the prediction of the peak gusts clearly benefits from the higher horizontal resolution (Fig. 24, shading). To simulate the observed gusts of up to 32 m/s over France, Germany and Switzerland a detailed description of the topography is neccessary.

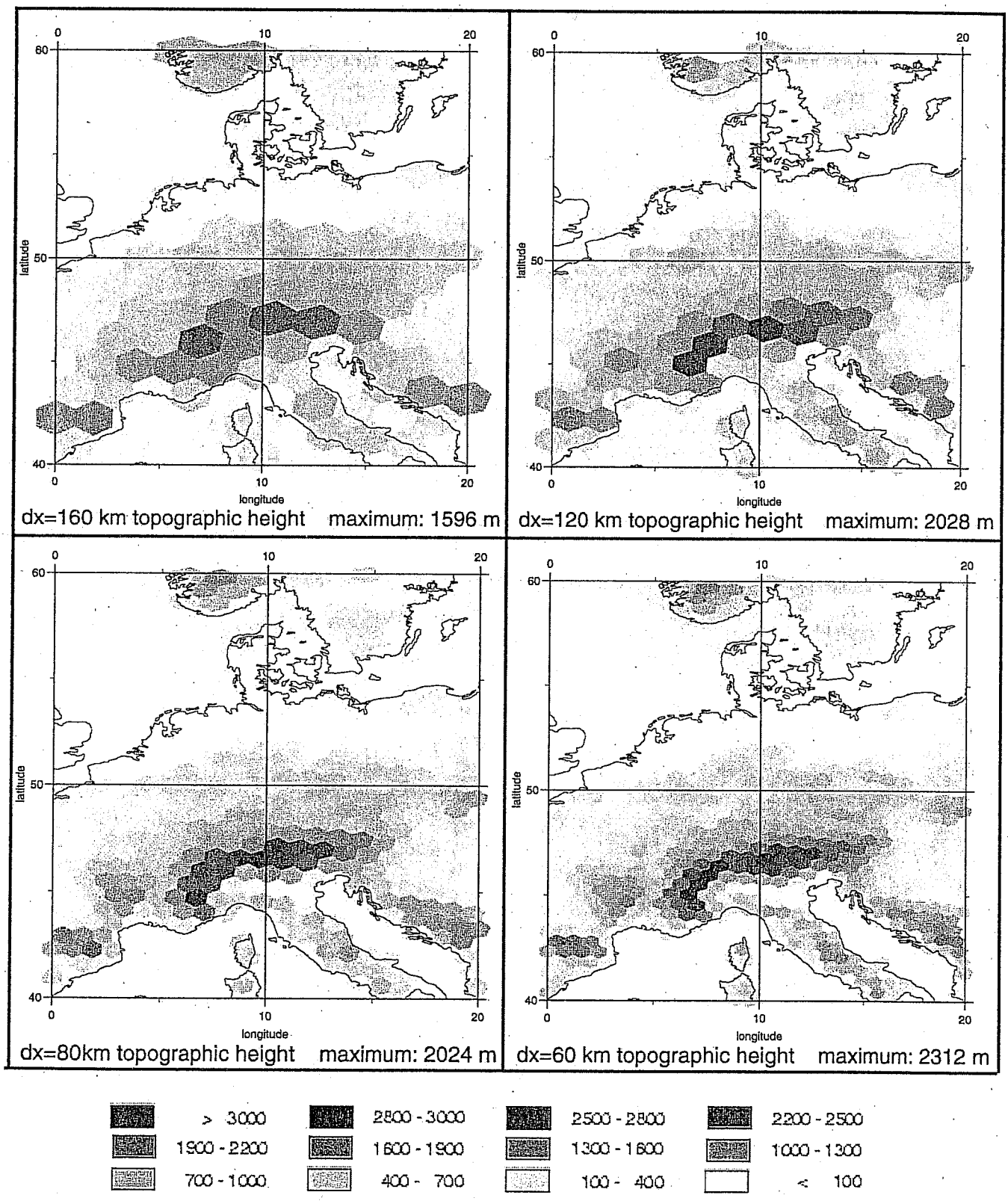

Figure 23 a Topography (unit: m) of the GME at different mesh sizes, namely 160 km (top left), 120 km (top right), 80 km (bottom left), 60 km (bottom right).

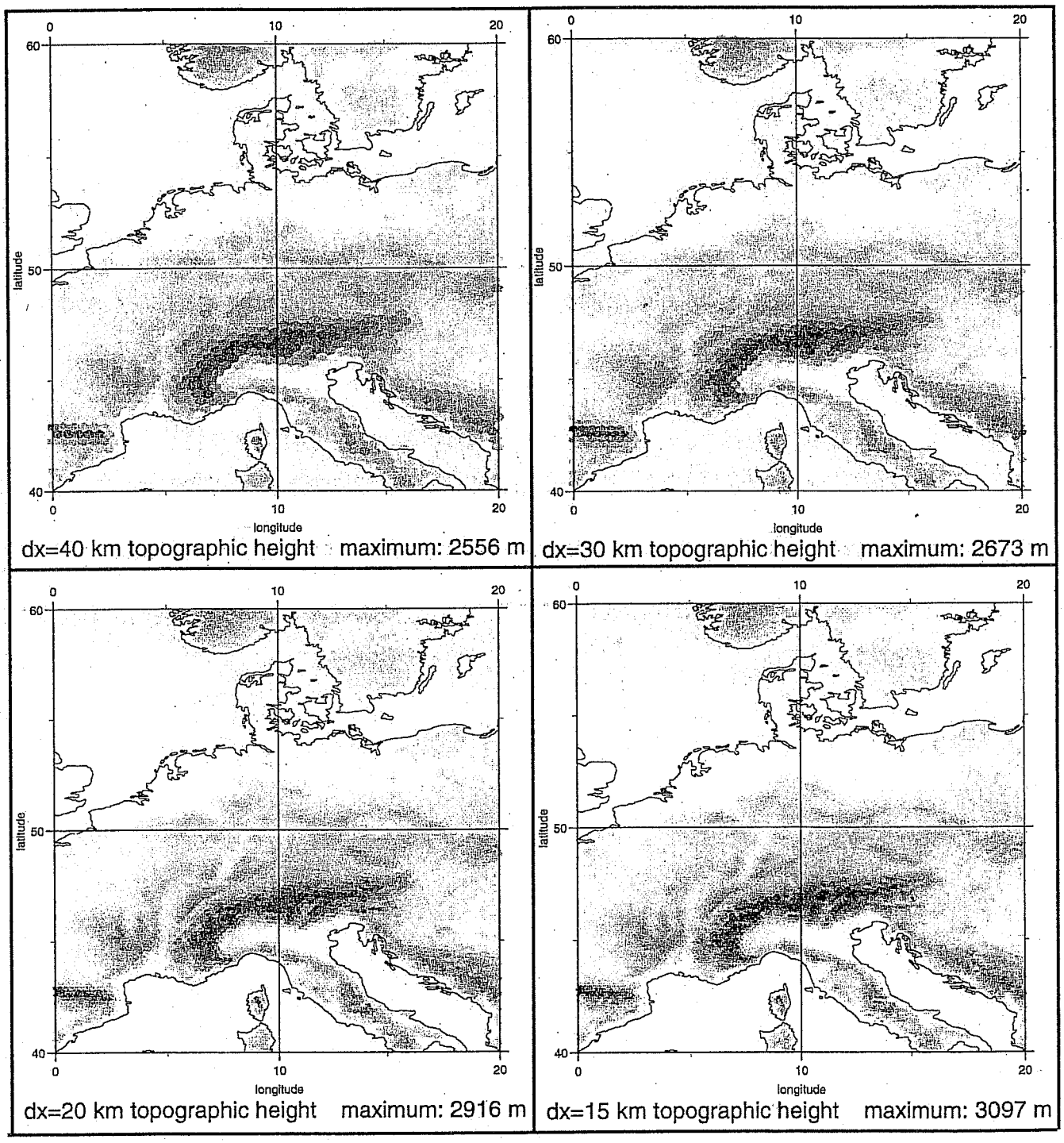

Figure 23 b Topography (unit: m) of the GME at different mesh sizes, namely 40 km (top left), 30 km (top right), 20 km (bottom left), 15 km (bottom right).

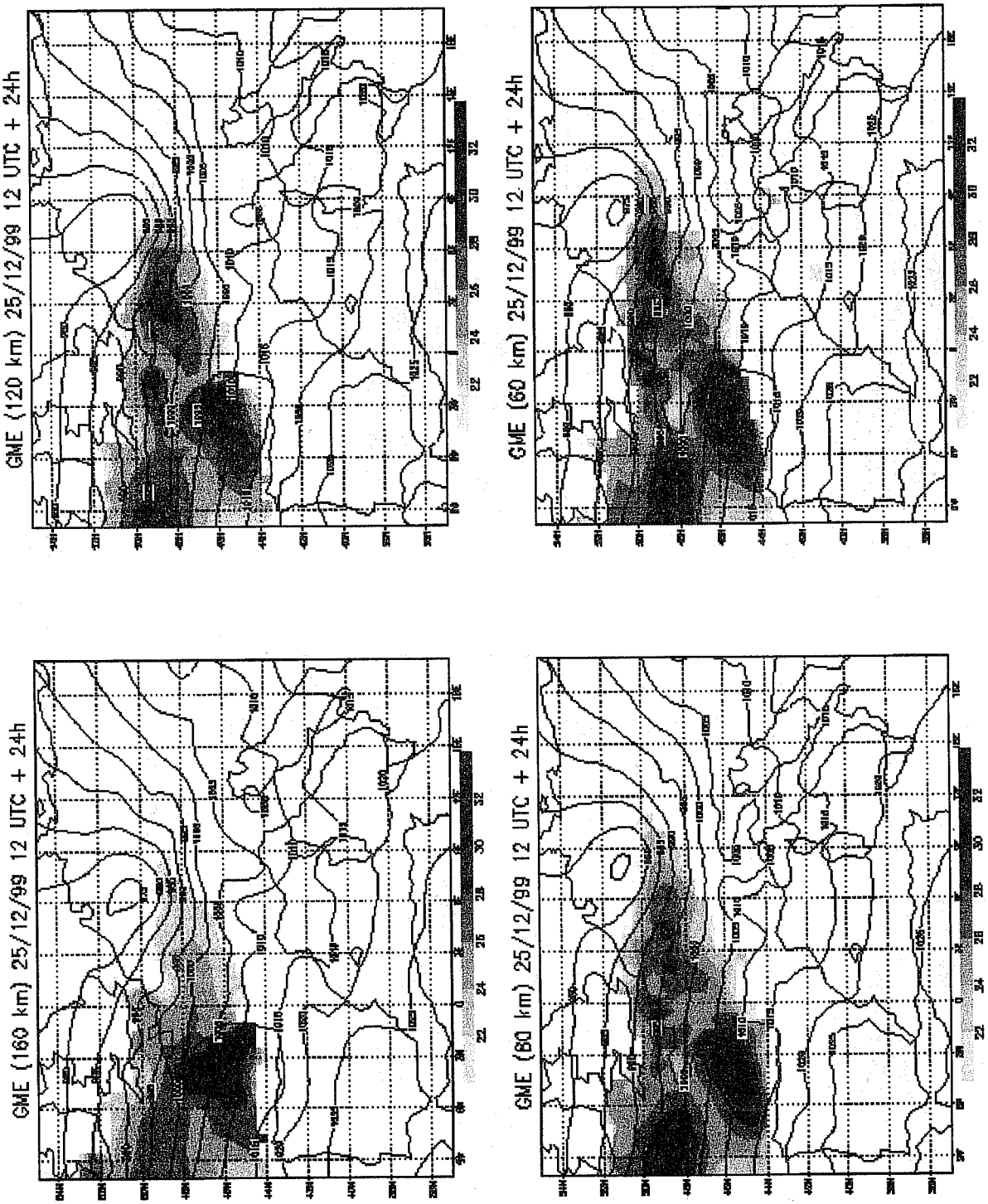

Figure 24a 24-h GME forecasts of mean sea level pressure (hPa) and maximum wind speed (m/s, shading) valid at 12 UTC on 26 Dec. 1999. Mesh sizes (clockwise): 160, 120, 80 and 60 km, 31 layers. Initial state: T106, 19 layers.

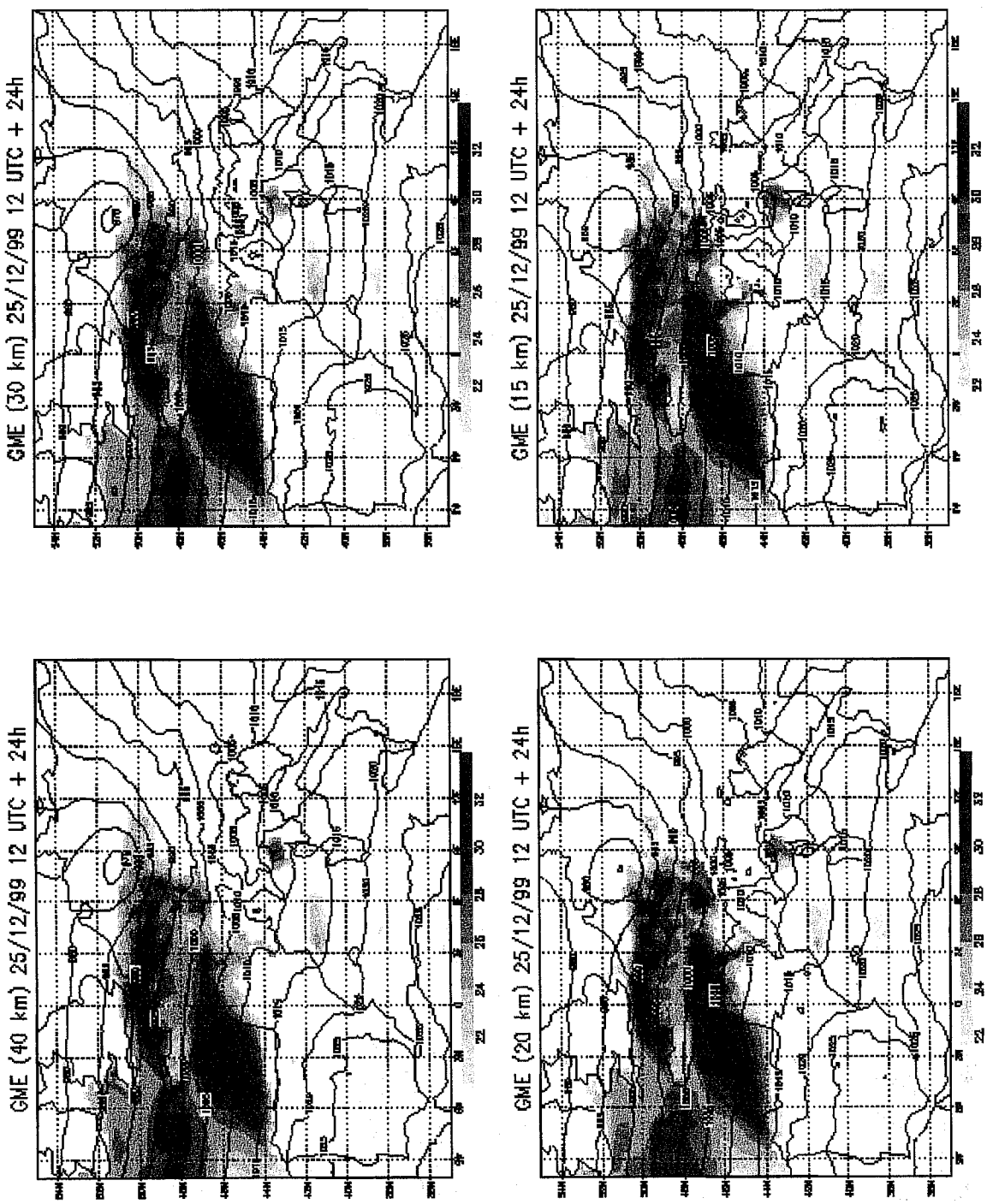

Figure 24b 24-h GME forecasts of mean sea level pressure (hPa) and maximum wind speed (m/s, shading) valid at 12 UTC on 26 Dec. 1999. Mesh sizes (clockwise): 40, 30, 20 and 15 km, 31 layers. Initial state: T106, 19 layers.

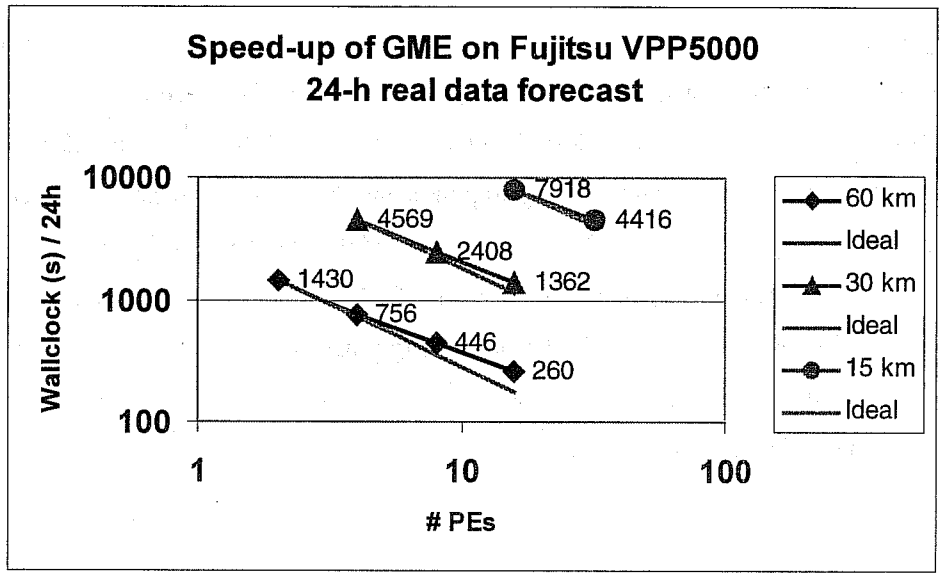

Figure 25 Speed-up of the GME at mesh sizes 60, 30, and 15 km of the Fujitsu VPP5000.

Fig. 25 shows the speed-up of the GME at different mesh sizes on the Fujitsu VPP5000. Obviously, there is some deviation from the linear speed-up. Probably the communication has to be optimised for this machine. Combining several short messages to larger ones will surely improve the performance of the GME on the VPP5000 considerably. Moreover, in the current version of the GME only one processor reads, unpacks and distributes the initial data file; at higher horizontal resolutions, this preparatory step takes up to 10% of the total wallclock time of a 24-h forecast.

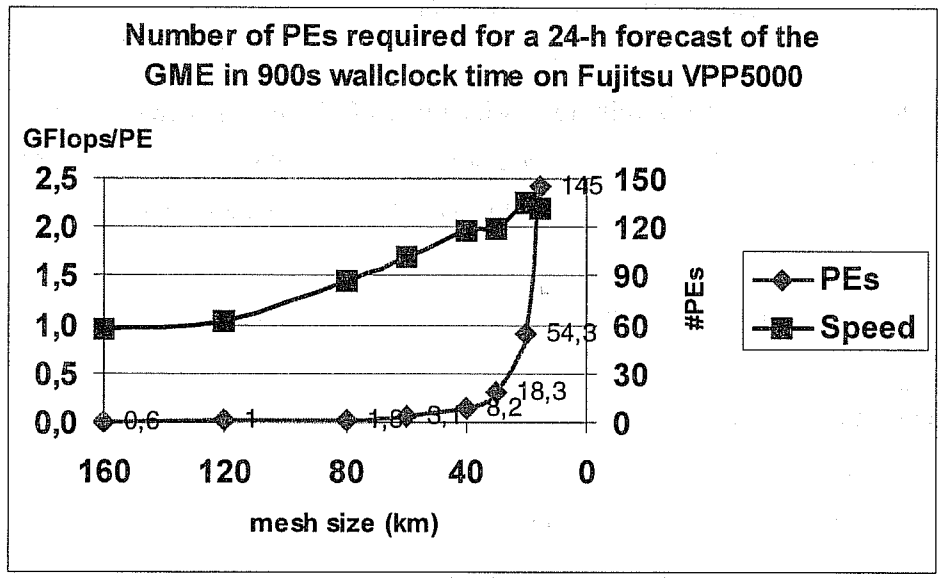

Figure 26 Number of processors required to perform a 24-h forecast in 900s wallclock time. Speed (GFlops) per PE on a Fujitsu VPP5000.

Allowing 15 minutes wallclock time for a 24-h forecast, just 3 Fujitsu VPP5000 processors are required at the current operational mesh size of 60 km, and about 54 processors will probably be sufficient at 20 km (Fig. 26). This is much less than the 3 x 3 x 3 x 3 = 81 processors derived from the simple scaling taking the increased number of grid points and the reduced timestep into account. At 15 km resolution, this corresponds to T_L1333 for a spectral model, more than 145 processors will be needed. Of course, current computing resources even at the ECMWF do not permit operational global forecasts at a resolution of 15 km. Not only the processing power is still insufficient, but the management of the huge analysis and forecast data files will push the systems to the limits. For example, at a mesh size of 15 km the initial data file exceeds 9 GByte!

8. SUMMARY AND OUTLOOK

With a small project team the DWD developed and implemented a new global model in just three years. In December 1999 the GME replaced the former spectral global model GM and the regional grid point model EM of the DWD, and became the first operational NWP model based on the icosahedral-hexagonal grid world wide.

The code is fully portable (Fortran90, MPI for message passing) and has been tested on several RISC and vector processors. Analysis and forecast data of the GME are used by ten national meteorological services world wide as initial and lateral boundary conditions for regional modelling. The GME system proved to be very reliable with no blow-ups so far.

The GME has been tested successfully for a wide range of mesh sizes between 160 and 15 km on the Fujitsu VPP5000 of the ECMWF. With current computer technology, a mesh size of 20 km, this corresponds to T_L1000 for a spectral model, would be feasible in operational applications.

From numerical and computational points of view, the future development of the GME will concentrate on

- an improvement of the numerical discretization of the Laplace operator to achieve fully second order accuracy,
- a better conservation of mass (for seasonal forecasts or climate mode runs),
- a faster solver of the Helmholtz equations, especially for the external mode,
- a semi-Lagrangian scheme allowing for Courant numbers greater than 1,
- better performance of the MPI communication by combining several short messages to larger ones, and finally
- a single-PE optimisation of the code.

Based on our experience and the expected improvements of the model in the future, it is probably justified to consider the icosahedral-hexagonal grid point approach as a serious alternative to currently employed methods for global models of the atmospheric flow.

9. ACKNOWLEDGEMENTS

We like to thank the following persons and institutions for their contribution to the development and first evaluation of the GME

• M. Gertz, DWD	Source code maintenance
• R. Johanni, SGI, Munich	MPI-Parallelisation of the GME
• D. Salmond, ECMWF	Code optimisation
• C. Jablonowski, Univ. Bonn	Held-Suarez test
• GMD, Birlinghoven	Design studies, shallow water tests
• P. Lynch, Ireland	Digital filtering initialisation
• S. Blessing, Univ. Hamburg	Case studies
• D. Grawe, Univ. Hamburg	Diagnostics
• T. Heinze, Univ. Bonn	Shallow water tests
• J. Koch, Univ. Freiburg	Helmholtz solver
• S. Maus, Univ. Mainz	Case studies, graphics
• J. Quaas, Univ. Köln	Smoothing operators
• J. Birkholz, Univ. Frankfurt	Kinetic energy spectrum

Moreover, thanks are due to all colleagues at the DWD who assisted in the operational implementation and validation of the model.

Mrs. Reiter took care of the manuscript.

10. REFERENCES

Baumgardner, J. R., 1983: A three-dimensional finite element model for mantle convection. Thesis, University of California, 271 pp.

Baumgardner, J. R. and P.O. Frederickson, 1985: Icosahedral discretization of the two-sphere. SIAM J. Numer. Anal., Vol. 22, No. 6, 1107-1115.

Burridge, D.M., 1975: A split semi-implicit reformulation of the Bushby-Timpson 10-level model. Quart. J. Roy. Meteor. Soc., 101, No. 430, 777-792.

Cullen, M. J., 1974: Integrations of the primitive equations on a sphere using the finite element method. Quart. J. Roy. Meteor. Soc., 100, No. 426, 555-562.

Doms, G. and U. Schättler, 1997: The nonhydrostatic limited-area model LM (Lokal-Modell) of DWD. Part I: Scientific Documentation. Deutscher Wetterdienst (DWD), Offenbach, March 1997.

Dutton, J.A., 1976: The ceaseless wind, McGraw-Hill, Inc., pp 579.

Giraldo, F. X., 1997: Lagrange-Galerkin methods on spherical geodesic grids. J. Comp. Phys., 136, 197-213.

Heikes, R. and D. A. Randall, 1995a: Numerical integration of the shallow-water equations on a twisted icosahedral grid. Part I: Basic design and results of tests. Mon. Wea. Rev., 123, 1862-1880.

Heikes, R. and D. A. Randall, 1995b: Numerical integration of the shallow-water equations on a twisted icosahedral grid. Part II: A detailed description of the grid and an analysis of numerical accuracy.
Mon. Wea. Rev., 123, 1881-1887.

Jacobsen, I. and E. Heise, 1982: A new economic method for the computation of the surface temperature in numerical models. Beitr. Phys. Atm., 55, No. 2, 128-141.

Lott, F. and M. Miller, 1997: A new sub-grid scale orographic drag parameterization: its formulation and testing. Quart. J. Roy. Meteor. Soc., 123, 101-128.

Louis, J.-F., 1979: A parametric model of vertical eddy fluxes in the atmosphere. Boundary-Layer Meteor., 17, 187-202.

Lynch, P., 1997: The Dolph-Chebyshev window: A simple optimal filter. Mon. Wea. Rev., 125, 655-660.

Majewski, D. 1998: The new global icosahedral-hexagonal grid point model GME of the Deutscher Wetterdienst, ECMWF, Seminar Proceedings, Recent developments in numerical methods for atmospheric modelling, 173-201.

Masuda, Y. and H. Ohnishi, 1986: An integration scheme of the primitive equations model with an icosahedral-hexagonal grid system and its application to the shallow water equations. Proc. WMO/IUGG Symp. on Short- and Medium-Range Numerical Weather Prediction. Tokyo, Japan, Japan Meteorological Society, 317-326.

Mellor, G.L. and T. Yamada, 1974: A hierarchy of turbulence closure models for planetary boundary layers. J. Atmos. Sci., 31, 1791-1806.

Müller, E., 1981: Turbulent flux parameterization in a regional-scale model. ECMWF Workshop on planetary boundary layer parameterization, 193-220.

Ritter, B. and J.-F. Geleyn, 1992: A comprehensive radiation scheme for numerical weather prediction models with potential applications in climate simulations. Mon. Wea. Rev., 120, 303-325.

Robert, A., 1981: A stable numerical integration scheme for the primitive meteorological equations. Atmos. Ocean, 17, 35-46.

Sadourny, R., A. Arakawa and Y. Mintz, 1968: Integration of the non-divergent barotropic vorticity equation with an icosahedral-hexagonal grid for the sphere. Mon. Wea. Rev., 96, 351-356.

Simmons, A. J. and D. M. Burridge, 1981: An energy and angular-momentum conserving vertical finite-difference scheme and hybrid vertical coordinate. Mon. Wea. Rev., 109, 758-766.

Staniforth, A. and J. Côté, 1991: Semi-Lagrangian integration schemes for atmospheric models – A review. Mon. Wea. Rev., 121, 2206-2223.

Stuhne, G. R. and W. R. Peltier, 1996: Vortex erosion and amalgamation in a new model of large scale flow on the sphere. J. Comput. Phys. 128, 58.

Stuhne, G. R. and W. R. Peltier, 1999: New icosahedral grid-point discretizations of the shallow water equations on the sphere. J. Comput. Phys. 148, 23-58.

Thuburn, J., 1997: A PV-based shallow-water model on a hexagonal-icosahedral grid.
Mon. Wea. Rev., 125, 2328-2347.

Tiedtke, M., 1989: A comprehensive mass flux scheme for cumulus parameterization in large-scale models.
Mon. Wea. Rev., 117, 1779-1800.

Williamson, D. L., 1968: Integration of the barotropic vorticity equation on a spherical geodesic grid. Tellus, 20, 642-653.